RSC Advances

PAPER

View Article Online
View Journal | View Issue



Cite this: *RSC Adv.*, 2026, **16**, 29172

# Synthesis, characterization, and application of magnetic novel nanofiber membranes for the removal of heavy-metal, organic and biological pollutants from wastewater

Şerife Saçmacı, *[ab] Rabia Güzel,[b] Mustafa Saçmacı,[c] Ruken Esra Demirdögen,[d] Aycan Gündogdu,[ef] Nuray Ateş,[gh] Oğuzhan Taştan,[b] Mefaret Ceylan,[b] Fatih Mehmet Emen[gh] and Kasim Ocakoglu[i]

In the present study, magnetic novel $NiFe_2O_4$:$Pr^{3+}$–MCM-41 (NiF:$Pr^{3+}$–M) and $CoFe_2O_4$:$Pr^{3+}$–MCM-41 (CoF:$Pr^{3+}$–M) nanofiber membranes were synthesized and used as effective and efficient adsorbents for magnetic dispersive micro-solid phase extraction (d-μSPE) and the removal of Cr, Pb, Ni, As, Al, Co, Cd, and Hg, as well as organic and microbial pollutants, from industrial wastewater. The nanofiber membranes of the (NiF:$Pr^{3+}$–M) and (CoF:$Pr^{3+}$–M) nanocomposites were prepared by the electrospinning method. The structural and morphological characterizations of the nanofiber membranes were performed by SEM, EDX, XRD, BET analysis, TGA and FT-IR spectroscopy. XRD analyses confirmed the formation of the spinel $NiFe_2O_4$ and $CoFe_2O_4$ phases, together with the preserved amorphous MCM-41 structure, while indicating the presence of Pr and Fe oxide secondary phases in both nanocomposites. The optimized experimental conditions for the pre-concentration of Cr, Pb, Ni, As, Al, Co, Cd, and Hg were as follows: for NiF:$Pr^{3+}$–M@PVDF, sample pH = 2; adsorption and elution contact time = 3 min; and eluent = 2 mol $L^{-1}$ $HNO_3$ (1 mL), while for CoF:$Pr^{3+}$–M@PVDF, pH = 4, adsorption and elution contact time = 3 min; and eluent = 2 mol $L^{-1}$ HCl (1 mL). The pre-concentration factor, detection limit, and precision of the method were determined. The recovery results obtained from the d-μSPE-ICP-MS procedure indicated that the nanofiber membranes served as highly efficient and effective adsorbents for the separation and pre-concentration of the elements at trace levels, as well as for the removal of organic and biological pollutants from wastewater. Thus, they can be exploited for various matrices, such as sea mucilage and tap water samples. The accuracy of the method was verified by analysis of the CWW-TMD wastewater Certified Reference Material.

Received 2nd March 2026
Accepted 7th May 2026

DOI: 10.1039/d6ra01796g

rsc.li/rsc-advances



## 1. Introduction

Water is one of the fundamental substances that support life and the natural environment. It is a primary component of industrial processes, a vital consumable item for humans and animals, and a vector for domestic and industrial pollution. The identification of new, potentially hazardous compounds in water has become a crucial task for water suppliers.[1]

Wastewater (a combination of liquid or water-carried waste removed from residences, institutions, and commercial and industrial establishments, together with ground water, surface water, and storm water) is defined as water that has been used by households, industries, and commercial establishments, which, unless treated, no longer serves a useful purpose and may contain contaminants.[2,3] It generally includes a high load of oxygen-demanding wastes, pathogenic or disease-causing agents, organic materials, nutrients that stimulate plant growth, inorganic chemicals, minerals, and sediments. It may also contain toxic compounds.[4] It comprises water from household sinks, washing machines, and kitchen appliances, as well as water flushed from toilets, and therefore, it contains a combination of nutrients and chemicals. Industrial contributions include carbon, nitrogen, and phosphorus nutrients, as

[a]*Department of Chemistry, Faculty of Sciences, Erciyes University, TR-38039, Kayseri, Türkiye. E-mail: sacmaci@erciyes.edu.tr; Fax: +90 352 4374933; Tel: +90 352 4374937*
[b]*Nanotechnology Research Center, Erciyes University, TR-38039, Kayseri, Türkiye*
[c]*Department of Chemistry, Faculty of Art & Sciences, Yozgat Bozok University, TR-66900, Yozgat, Türkiye*
[d]*Department of Chemistry, Faculty of Science, Çankırı Karatekin University, TR-18100, Çankiri, Türkiye*
[e]*Genome and Stem Cell Center, Erciyes University, TR-38039, Kayseri, Türkiye*
[f]*Department of Immunology, School of Medicine, Istanbul Medeniyet University, TR-34700, İstanbul, Türkiye*
[g]*Department of Environmental Engineering, Faculty of Engineering, Erciyes University, TR-38039, Kayseri, Türkiye*
[h]*Department of Inorganic Chemistry, Faculty of Science and Literature, Mehmet Akif Ersoy University, Burdur, Türkiye*
[i]*Department of Engineering Fundamental Sciences, Faculty of Engineering, Tarsus University, Tarsus 33400, Türkiye*

well as pesticides and other chemicals, depending on the specific industry.[5] When left untreated, these nutrients and chemicals enter natural water systems where they harm the environment and human health.[6]

A host of bacterial, viral, and protozoan organisms can survive in human waste and fecal matter. These include *Escherichia coli*, which can be present in pathogenic form in wastewater.[7] In ecosystems, nutrient pollution can lead to algal blooms and eutrophication, as excess nutrients allow aquatic microorganisms to proliferate and consume all available oxygen, ultimately depleting the water's oxygen content. Eutrophication can lead to fish deaths due to the formation of anoxic conditions.[6] Humans are also at risk of shellfish poisoning from the accumulation of biological contaminants in filter-feeding organisms.[8,9] Other effects, such as the emerging issue of endocrine disruption in organisms, can occur in part due to the presence of pharmaceutical products or chemicals in waterways.[6]

Water sources are particularly vulnerable to pollution. Polluted water has a profound impact on the health of communities, the sustainability of aquatic ecosystems, the natural environment, and the economic and social well-being of society. For example, it has been reported that inadequate water supplies, in terms of both quantity and quality, coupled with poor sanitation globally, account for the death of approximately 30 000 people per day. Of these cases, 80% occur in rural areas, with the highest percentage occurring among infants.[10]

The most common pollutants present in wastewater are metal ions, anions, dyes, phenols, pesticides, detergents, and a broad spectrum of aromatic compounds. The presence of these contaminants in wastewater can render natural water unfit for drinking purposes and also toxic to aquatic life. Several processes have been applied, with varying degrees of success, to treat water and wastewater. These processes include coagulation, filtration, ion exchange, anaerobic treatment, advanced oxidation, electrolysis, and non-MNP-based adsorption techniques. These treatment options can be used to remove contaminants from water. However, several factors hinder their application, including insufficient pollutant removal, difficult adsorbent recovery, and high cost. In some cases, the waste sludge is voluminous, requiring a proper design and a large amount of space for disposal.[11–13]

The exploration of nanomaterials is an active research area in magnetic d-μSPE. These new materials, as adsorbents, are essential for obtaining more selective materials, increased adsorption capacities, high specific surface areas, and improved chemical stability.[14] Nanoparticles exhibit enhanced reactivity, a large surface area, and accelerated sorption kinetics, possessing unique thermal, mechanical, and electronic properties.[15]

In recent years, magnetic nanoparticles (MNPs) have garnered considerable attention due to their unique superparamagnetic (SPM) properties, high adsorption capacities, and surface area-to-volume ratio.[14] In particular, transition metal oxides with spinel structures, commonly referred to as ferrites, are among the most essential MNPs. Based on their crystal structures and magnetic properties, ferrites are classified as spinel ($MFe_2O_4$, where M = Mn, Fe, Co, Ni, Co, Zn, *etc.*), garnet ($M_3Fe_5O_{12}$, where M = rare earth cations), hexaferrite ($SrFe_{12}O_{19}$ and $BaFe_{12}O_{19}$) and orthoferrite ($MFeO_3$, M = rare earth cations).[16–18] Among these, special attention has been given to spinel ferrite nanoparticles (SFNPs) due to their excellent magnetic properties, simple chemical composition, and wide range of applications in various fields, including water and wastewater treatment, biomedicine, catalysis, and electronic devices.[16] When hazardous substances have to be measured at low levels (for health or precautionary reasons), the measurements should be reliable.

Therefore, there is a need for an adsorbent that is low-cost, efficient, easily recovered, and reusable. Hence, SFNPs/SFNCs appear to be attractive materials that can provide the desired solutions to the problems pertaining to water purification and quality.[19–21] This is primarily due to their exceptional physical and chemical properties, which facilitate recovery and re-use, as well as their ability to remove a wide range of contaminants simultaneously.

In this study, magnetic NiF:$Pr^{3+}$–M@PVDF and CoF:$Pr^{3+}$–M@PVDF nanofiber membranes were synthesized and investigated for the first time as adsorbents for the separation/preconcentration of Cr, Pb, Ni, As, Al, Co, Cd, and Hg elements from wastewater, sea mucilage, and tap water samples. An electrospinning device was used to obtain the nanofiber membranes. The structural characterization of the prepared NiF:$Pr^{3+}$–M and CoF:$Pr^{3+}$–M nanocomposites and nanofiber membranes (NiF:$Pr^{3+}$–M@PVDF and CoF:$Pr^{3+}$–M@PVDF) was carried out by SEM, EDX, XRD, BET, TGA and FT-IR analyses. The parameters, including sample pH, adsorption and elution contact times, eluent concentration and volume, sample volume, and effects of interfering ions, were optimized for the determination of Cr, Pb, Ni, As, Al, Co, Cd, and Hg. The adsorption capacity of the magnetic nanofiber membranes and their reusability performance were investigated.

## 2. Materials and methods

### 2.1. Reagents

The following high-purity (99.9%) reagents were used in all experiments: iron(III) chloride ($FeCl_3 \cdot 6H_2O$, 99%, Merck), nickel(II) chloride ($NiCl_2 \cdot 4H_2O$, 99.9%, Merck), acetone ($C_3H_6O$, 99%, Merck), *N*,*N*-dimethylformamide (DMF, $C_3H_7NO$, 99%, Merck), dimethyl sulfoxide (DMSO, $C_2H_6SO$, 99%, Sigma), aqueous solution of ammonia ($NH_4OH$, 25% (v/v), Merck), praseodymium nitrate ($Pr(NO_3)_3 \cdot 6H_2O$, 99%, Aldrich), cetyltrimethylammonium bromide (CTAB, $C_{16}H_{33}(CH_3)_3NBr$, 98%, Sigma), tetraethyl orthosilicate (TEOS, $C_8H_{20}OSi$, 98%, Aldrich), ethanol (EtOH, $C_2H_5OH$, 96%, Merck), boron nitride (BN, powder, ~1 μm, 98%, Merck), oxalic acid ($C_2H_2O_4 \cdot 2H_2O$, 99%, Merck), propylene glycol ($CH_3CH(OH)CH_2OH$, 99%, Sigma), and poly(vinylidene fluoride) (PVDF, $-(C_2H_2CF_2)_n-$, average $M_w \approx 534\,000$ by GPC powder, Aldrich).

Ultrapure water (18.2 MΩ $cm^{-1}$ resistivity) was obtained from the Milli-Q system (Millipore, USA) and used in all experiments. A high-purity ICP-MS multi-element standard solution (10 mg $L^{-1}$) obtained from Merck (Darmstadt,

Germany) was used to prepare the calibration curves. Laboratory glassware was kept overnight in a dilute $HNO_3$ solution (1 : 1) and then rinsed with ultrapure water before the experiments until the washings reached a neutral pH.

Test solutions were prepared daily from stock solutions for all pH values studied using the following relevant solutions: 0.1 mol $L^{-1}$ of NaOH and 0.1 mol $L^{-1}$ of $HNO_3$ for pH 1–10. Additionally, 2 mol $L^{-1}$ of $HNO_3$ and 2 mol $L^{-1}$ of HCl were used as eluents throughout the experiments. The CWW-TMD wastewater (mg $L^{-1}$) Certified Reference Material was used to study the accuracy of the method.

### 2.2. Sample collection and processing

For experimental tests, wastewater samples were collected weekly for fourteen weeks from January 2022 to April 2022, from the treated and untreated wastewater samples collected from the Industrial Area in Kayseri's advanced biological wastewater treatment plant. All samples were collected between 09:00 am and 11:00 am on the same day of the week using a grab-sampling technique. The sea sample was directly collected from locations in the Marmara Sea (Istanbul) and analyzed without pre-treatment. Tap water samples were collected from our research laboratory (in Kayseri) and analyzed without pre-treatment.

For the analysis of trace metals, 1 L portions of wastewater and sea samples collected were stored in polyethylene bottles (mechanically cleaned, *i.e.*, pre-washed with detergent, ultrapure water, dilute $HNO_3$, and ultra-pure water, sequentially). The wastewater samples were filtered through a cellulose membrane filter (Schleicher & Schuell, Dassel, Germany) with a pore size of 0.45 μm (0.45 μm porosity, 47 mm diameter; Advantec MFS, Inc., CA, USA), and then, the procedure reported in the literature was immediately applied as soon as the samples arrived at the laboratory.[22] The concentrations of the elements (Cr, Pb, Ni, As, Al, Co, Cd, and Hg) in the filtered samples (1 mL) were determined by ICP-MS after applying the optimized method (the method detailed in Section 2.6).

The microbiological analyses of the species present in untreated (influent) wastewater samples collected from the wastewater treatment plant weekly were carried out over three weeks (April 2022). The wastewater was collected using 500 mL sterile microbiological containers mounted on a handle approximately 1–1.5 m in length, allowing for safe sampling from the influent stream without operator contact. All samples were transported under cold-chain conditions and processed in the laboratory within 4 hours of sampling. Sample processing was performed in accordance with the accepted method given elsewhere.[23] To avoid misleading or non-quantifiable results, *E. coli* enumeration was conducted exclusively on influent (untreated wastewater) samples because untreated influent carries the highest and most stable microbial load, ensuring accurate and reproducible colony enumeration.

The success of the organic-matter removal efficiency of the novel NiF:$Pr^{3+}$–M@PVDF and CoF:$Pr^{3+}$–M@PVDF nanofiber membranes was tested by determining the chemical oxygen demand (COD) in the treated and untreated wastewater samples collected from the wastewater treatment plant during weeks 1–12 and in week 15. The efficiency of sorption of the thus-produced nanofiber membranes in the removal of organic pollutants was determined by introducing nanofibers containing 25 mg of NiF:$Pr^{3+}$–M@PVDF and 100 mg of CoF:$Pr^{3+}$–M@PVDF into the wastewater sample. The nanofiber membranes were allowed to interact with the wastewater for predetermined contact times of 20 and 50 min. Then, the samples were subjected to COD analysis to determine the efficiency of organic pollutant removal.

### 2.3. Instrumentation

Measurements were performed using an inductively coupled plasma mass spectrometer (ICP-MS Agilent 7500a, Agilent Technologies, Tokyo, Japan) equipped with an autosampler, a Babington nebulizer, nickel cones, and a peristaltic sample delivery pump. The system was used for the simultaneous multi-element detection of Cr, Pb, Ni, As, Al, Co, Cd, and Hg. The ICP-MS operating conditions are given in Table 1.

Analysis of each sample was performed in triplicate. High-purity argon gas was used to form plasma in the ICP-MS. Agilent ICP-MS tuning solution of 10 μg $L^{-1}$ (Ce, Co, Li, Tl, and Y) was used for the tuning of the instrument. Data acquisition was performed in both spectrum analysis and full quantitative modes.

The surface morphologies of the synthesized novel nanocomposites, *i.e.*, the as-prepared Ni/CoF:$Pr^{3+}$–M, were imaged by scanning electron microscopy (SEM; ZEISS EVO LS10) at 25

Table 1 Operating conditions for ICP-MS (Agilent 7500a)

| | |
|---|---|
| Nebulizer | Babington type |
| Spray chamber | Quarts, double pass |
| RF generator | Frequency: 10 MHz and power output: 1220 W |
| Ar flow rate (L $min^{-1}$) | 20 |
| Auxiliary gas flow rate (L $min^{-1}$) | 0.9 |
| Nebuliser gas flow rate (L $min^{-1}$) | 1–1.2 |
| Sample uptake rate(L $min^{-1}$) | 400 |
| Number of replicates | 3 |
| Integration time (s) | 0.1 |
| Internal standards | Bi, Rh, and Sc |
| Isotopes | The following isotopes of trace elements were considered: $^{27}Al$, $^{53}Cr$, $^{60}Ni$, $^{75}As$, $^{111}Cd$, $^{201}Hg$, $^{59}Co$ and $^{208}Pb$ |

kV and energy dispersive X-ray spectroscopy (EDX, Bruker). The elemental analysis was performed using energy-dispersive X-ray (EDX, Bruker) spectroscopy coupled with SEM. The crystal structures of the as-prepared Ni/CoF:$Pr^{3+}$–M were analyzed *via* X-ray thin-film diffraction analysis (XRD), and the pattern was collected using a PANalytical Empyrean diffractometer with a Cu K$\alpha$ radiation source ($\lambda = 0.154$ nm) operated at 45 kV and 40 mA, in the range of 1° to 90°. High Score Plus search-match software was used for phase determination. The BET surface area and porosity of the nanofilter membranes were determined by the BET-$N_2$ method using a Micromeritics Gemini VII analyzer (Norcross, USA). Thermogravimetric analysis (TGA) curves were obtained using a HITACHI STA 7300 TG/DTA thermal analyser under a dynamic air atmosphere. A sample size of 4–5 mg and a heating rate of 10 °C $min^{-1}$ in the temperature range of 0 °C-1000 °C were used.

The FT-IR spectra were recorded using a PerkinElmer Spectrum (400 FT-IR Spectrometer Spotlight 400 Imaging System). The FT-IR measurements were performed in the 4000–400 $cm^{-1}$ range using the ATR mode to analyze bond characteristics.

The Ultrasonic HD 2070 Bandelin Sonopuls Ultrasonic Homogenizer (Germany) was used to obtain homogeneous solutions for synthesizing the nanofiber membranes of Ni/CoF:$Pr^{3+}$–M@PVDF. The near-field electrospinning device (NFS40) used was obtained from Eraktek.

### 2.4. Preparation of $NiFe_2O_4$:$Pr^{3+}$–MCM-41 and $CoFe_2O_4$:$Pr^{3+}$–MCM-41 nanocomposites

The MCM-41 (M) sample used in this study was synthesized according to a hydrothermal synthesis procedure, as described in a previous study.[24] Briefly, 0.50 g of CTAB (as a surfactant) was dissolved in 100 mL of ultra-pure water. Into this mixture, 35 mL of ethanol, 10 mL of an $NH_3$ solution (3 mol $L^{-1}$), and 2 mL of TEOS (as a silica source) were added. The solution was stirred at room temperature for 3 h until a white precipitate was obtained. Then, the precipitate was filtered and washed with ultra-pure water and ethanol, followed by drying in air. Thereafter, it was calcined in the furnace at 550 °C for 10 hours.

First, the $NiFe_2O_4$:$Pr^{3+}$ (NiF:$Pr^{3+}$) nanocomposite was synthesized according to the method given elsewhere.[25] A solid mixture of $NiCl_2 \cdot 6H_2O$ (1 mmol), $FeCl_3 \cdot 6H_2O$ (2 mmol), and $Pr(NO_3)_3 \cdot 6H_2O$ (1 mmol) was dissolved in 100 mL of ultra-pure water and stirred until a dark-green-colored solution formed. Then, a mixture of oxalic acid and propylene glycol (30 mmol) was added to the solution and heated at 80 °C for 3 hours to form a gel. The obtained product was then placed in a muffle furnace and calcined at 800 °C for 2 hours.

Next, the $CoFe_2O_4$:$Pr^{3+}$ (CoF:$Pr^{3+}$) nanocomposite was synthesized by the starch-assisted sol–gel auto-combustion method.[24] Stoichiometric amounts of $CoCl_2 \cdot 6H_2O$ (1 mmol), $FeCl_3 \cdot 6H_2O$ (2 mmol), and $Pr(NO_3)_3 \cdot 6H_2O$ (1 mmol) were dissolved in 100 mL of ultra-pure water and stirred for 30 min. An aqueous solution of starch (10 mmol) was used as a fuel and was added to the above solution, which was then stirred at 50 °C for 1 h. An aqueous ammonia solution (3 mol $L^{-1}$) was then added dropwise under constant stirring until the pH remained constant at ~7.0 at room temperature. The mixed solution was heated on a hot plate at 100 °C for 4 hours. During evaporation, the solution turned into a viscous brown gel. Then, the gel was placed in a preheated oven at 200 °C. The auto-combustion process started in the hottest zones and propagated upward, similar to the eruption of a volcano, through self-ignition. The gel completely burned, forming a powder. The powder obtained was ground in an agate mortar until it was completely homogenized. The burned powder material was calcined in the furnace at 700 °C for 2 hours.

The synthesis of $Pr^{3+}$–nickel/cobalt ferrite (Ni/CoF:$Pr^{3+}$) nanocomposites with M was done *via* the wet impregnation method. For this, 1.0 g of the Ni/CoF:$Pr^{3+}$ nanocomposites was added to a mixture of 10 mL of deionized water and 50 mL of ethanol. After dispersing the solution *via* sonication for 30 min, 2.5 mL of aqueous ammonia (3 mol $L^{-1}$) and 0.85 g of M were added. The mixture was stirred for an additional 24 hours at room temperature. The obtained Ni/CoF:$Pr^{3+}$:M nanocomposites were separated using an external magnet and then rinsed with ultra-pure water and ethanol. Finally, the nanocomposites were dried at 80 °C under vacuum for 12 h.

### 2.5. Synthesis of the NiF:$Pr^{3+}$–M@PVDF and CoF:$Pr^{3+}$–M@PVDF nanofiber membranes

A solution of PVDF was prepared by dissolving 0.5 g of PVDF in a 10 mL DMF : acetone (2 : 1, v/v) solution at 50 °C, followed by stirring for 12 h to form a homogeneous suspension. At the same time, 5.0 mg of boron nitride (BN) and 0.05 g of the Ni/CoF:$Pr^{3+}$–M nanocomposites were dispersed in 5.0 mL of DMF/acetone using a sonicator for 1 h, separately. Then, they were added to the PVDF solution, and all the mixtures were sonicated at 70 W for 3 h. Subsequently, PVDF/BN-coated Ni/CoF:$Pr^{3+}$–M nanocomposites were collected using a permanent magnet and washed three times with ultra-pure water. The precipitates obtained were dried in an oven at 80 °C for 1 h. The reaction synthesis scheme of this process is given in Fig. 1.

Nanofiber membranes were obtained *via* electrospinning of solutions prepared by dissolving novel Ni/CoF:$Pr^{3+}$–M nanocomposites in a DMSO : acetone mixture (1 : 1), with mixing achieved *via* magnetic stirring for 1 h at 500 rpm at room temperature. The parameters for the electrospinning process were optimized as follows: a voltage of 15 kV, an injection pump speed of 0.1 mL $h^{-1}$ at room temperature, and a distance of 11 cm between the needle tip and the collector (see Fig. 1).

### 2.6. Analytical procedure

The developed method was successfully applied to the ICP-MS measurements for the determination of Cr, Pb, Ni, As, Al, Co, Cd, and Hg in wastewater, sea mucilage, and tap water samples. For this reason, two different NiF:$Pr^{3+}$–M@PVDF and CoF:$Pr^{3+}$–M@PVDF nanofiber membranes were used in the study, and the obtained results were compared.

The method was optimized with wastewater solutions before it was applied. 25 mL portions of the wastewater examples were placed in centrifuge tubes. 25 mg of NiF:$Pr^{3+}$–M@PVDF and 100 mg of CoF:$Pr^{3+}$–M@PVDF were separately placed in a 50 mL

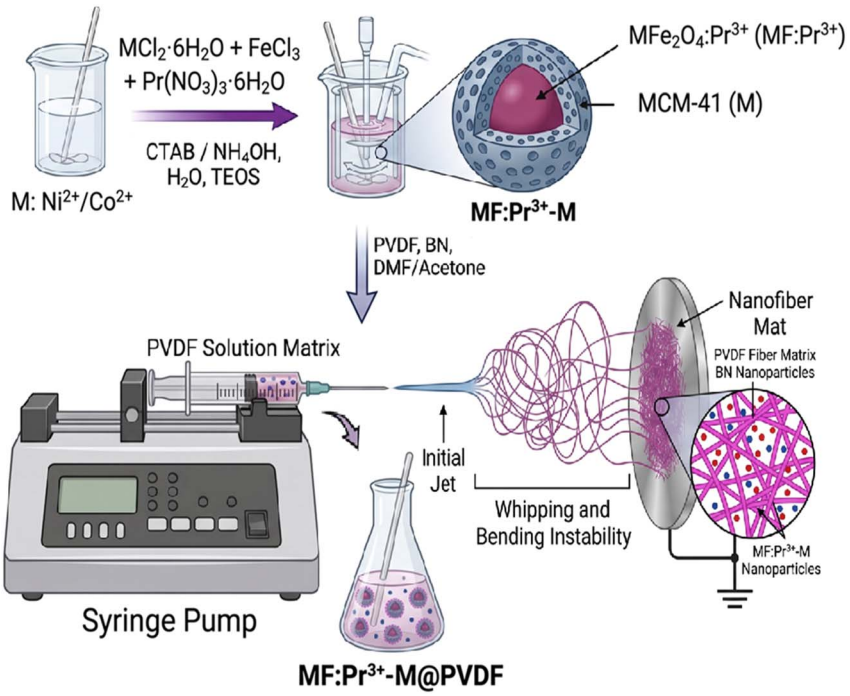


Fig. 1 Schematic of the synthesis of the MF:$Pr^{3+}$–MCM-41@PVDF nanoparticles with MF: $Pr^{3+}$, MCM-41, BN, and PVDF.

centrifuge tube as sorbent materials. The pH of the solutions was adjusted to 2.0 using 0.1 mol $L^{-1}$ of an $HNO_3$/NaOH solution for the NiF:$Pr^{3+}$–M@PVDF nanofiber membrane and to pH 4.0 using 0.1 mol $L^{-1}$ of the $HNO_3$/NaOH solution for the CoF:$Pr^{3+}$–M@PVDF nanofiber membrane. The mixtures were vortexed for 3 min. Then, the nanofiber membranes were separated using a strong magnet, and the supernatant was carefully decanted using a pipette. 1 mL of 2 mol $L^{-1}$ $HNO_3$ was used for the elution of NiF:$Pr^{3+}$–M@PVDF, while 1 mL of 2 mol $L^{-1}$ HCl was used for the elution of CoF:$Pr^{3+}$–M@PVDF. After vortexing for 3 minutes, the nanofiber membranes were separated from the eluent using a magnet. The concentration of the elements in the eluent (Cr, Pb, Al, As, Co, Ni, Cd, and Hg) was determined by ICP-MS. The magnetic d-μSPE was applied to wastewater, sea mucilage, and tap water samples for blank analysis.

### 2.7. Procedure of BOD analysis

Samples were analyzed in accordance with international standards, as outlined in the Australian and New Zealand Standards for Water Microbiology and Water Quality Sampling (Australian and New Zealand Standards 2007).[23] *E. coli* enumeration in wastewater before treatment was assessed *via* a membrane filtration system. Sterile 0.45 μm pore-size nitrate cellulose filters (Millipore) were used to filter 10 mL and 20 mL of the water samples. The filters were plated on membrane thermotolerant *E. coli* agar (mTEC agar, Oxoid) and incubated at 35 °C for 2 hours, followed by 24 hours at 44 °C. Colonies exhibiting a purplish-red color were identified as *E. coli*, and the colony counts were subsequently expressed as CFU $mL^{-1}$ by normalizing to the filtered volume. For each sample, triplicate plating was performed to ensure accuracy and reproducibility of colony enumeration. The colony-forming units (CFU) were counted per milliliter (CFU $mL^{-1}$) for each of the three plates, and the final reported value was obtained by calculating the mean of these triplicate counts.

### 2.8. Procedure of COD analysis

Chemical oxygen demand (COD) determination was performed using the SM 5220 D closed reflux–colorimetric method, as outlined in Standard Methods (APHA, AWWA, WEF, 2017).[26] Before starting the analysis, the wastewater samples were shaken to ensure complete homogeneity, and appropriate dilutions were made when the wastewater COD concentration was above the calibration range. A 2.5 mL wastewater sample, 1.5 mL of a potassium dichromate solution ($K_2Cr_2O_7$), and 3.5 mL of a silver sulfate–sulfuric acid mixture ($AgSO_4$–$H_2SO_4$) were added sequentially to the COD tubes. Then, the COD tubes were capped immediately, and a short vortex was applied (10 s) to ensure homogeneous distribution of the contents. Closed tubes were digested for 120 minutes in a thermo reactor that had been previously preheated to 150 °C.

After the digestion process was completed, the tubes were removed from the thermo reactor and allowed to cool to room temperature. The absorbance of the cooled tubes was measured on a UV-Vis spectrophotometer at a 600 nm wavelength. The COD content of the wastewater samples was determined by plotting absorbance values *versus* concentration, which produced a calibration curve. The calibration curve was prepared in two different calibration ranges as low (0, 25, 50, 75, 100, 125, 150 mg $L^{-1}$) and high (0, 100, 200, 400, 600, 800, 1000 mg $L^{-1}$) using potassium hydrogen phthalate (KHP,

 

$C_8H_5KO_4$), in accordance with Standard Methods 5220 D. Standard COD solutions of known concentrations were prepared following the same digestion procedure applied to the samples, and ultrapure water was used as a blank.

## 3. Results and discussion

### 3.1. Characterization of the Ni/CoF:$Pr^{3+}$–M nanocomposite

The XRD patterns of the NiF:$Pr^{3+}$ and NiF:$Pr^{3+}$–M are presented in Fig. 2(a). Both samples exhibit diffraction peaks corresponding to the characteristic spinel reflections of $NiFe_2O_4$, in agreement with JCPDS card no. 10-0325.[27] The main reflections located at the (220), (311), (400), (422), (511), and (440) planes confirm that the spinel phase is formed in both the free powder sample (NiF:$Pr^{3+}$) and the MCM-41-supported sample (NiF:$Pr^{3+}$–M). In addition to the spinel peaks, both samples display several secondary reflections assigned to α-$Fe_2O_3$, FeO and $PrFeO_3$, indicating that the introduction of $Pr^{3+}$ at a molar ratio equal to $Ni^{2+}$ results in the formation of a multi-phase composite rather than a fully Pr-doped single-phase spinel structure. The consistent presence of these impurity phases in both NiF:$Pr^{3+}$ and NiF:$Pr^{3+}$–M suggests that the phase separation originates from the overall composition rather than the synthesis environment or support. For NiF:$Pr^{3+}$–M, which represents partially

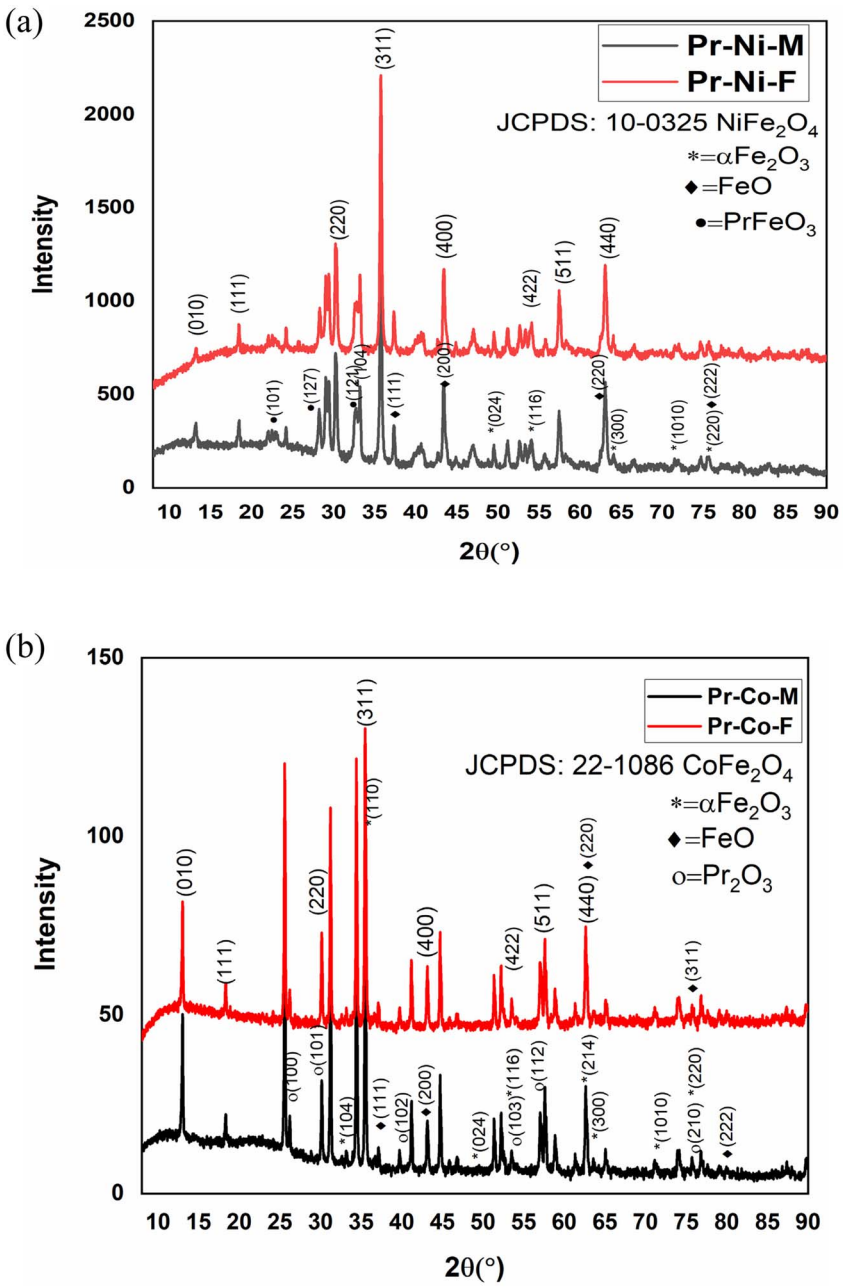


Fig. 2 (a) XRD patterns of $NiFe_2O_4$:$Pr^{3+}$ (Pr–Ni–F) and $NiFe_2O_4$:$Pr^{3+}$–MCM-41 (Pr–Ni–M). (b) XRD patterns of $CoFe_2O_4$:$Pr^{3+}$ (Pr–Co–F) and $CoFe_2O_4$:$Pr^{3+}$–MCM-41 (Pr–Co–M).

Pr-doped $NiFe_2O_4$ nanoparticles incorporated into the mesoporous channels of MCM-41, the diffraction peaks exhibit significantly reduced intensities compared to those for NiF:$Pr^{3+}$. This reduction is attributed to the high dispersion of nanoparticles within the silica framework and the partial amorphous background of MCM-41, which collectively decrease the overall crystallinity. Moreover, the broad amorphous halo centred around $2\theta \approx 22°–25°$—a typical feature of the disordered silica walls—confirms that the MCM-41 structure is preserved after nanoparticle incorporation.

Nevertheless, the identical impurity peaks observed in both samples demonstrate that the confined environment of MCM-41 does not prevent the formation of secondary phases, such as $PrFeO_3$ and Fe-oxide species. The likely origin of this multi-phase formation is the excessive $Pr^{3+}$ content relative to the tolerance of the spinel lattice. Because $Pr^{3+}$ has a substantially larger ionic radius compared to $Ni^{2+}$ and $Fe^{3+}$, the spinel structure cannot fully accommodate $Pr^{3+}$ ions, causing the excess Pr to segregate into separate Pr-containing oxide phases. Simultaneously, deviations in the Fe oxidation balance may promote $\alpha$-$Fe_2O_3$ and FeO crystallization. Overall, the XRD results indicate that both NiF:$Pr^{3+}$ and NiF:$Pr^{3+}$–M samples consist of $NiFe_2O_4$ as the primary phase, accompanied by $PrFeO_3$ and Fe-oxide impurities, confirming the formation of a multi-phase system rather than a pure Pr-doped spinel. The incorporation of nanoparticles into MCM-41 influences crystallinity but does not alter the fundamental phase composition. Furthermore, the detection of the characteristic amorphous MCM-41 background peak demonstrates that the mesoporous support remains structurally intact following impregnation and calcination.

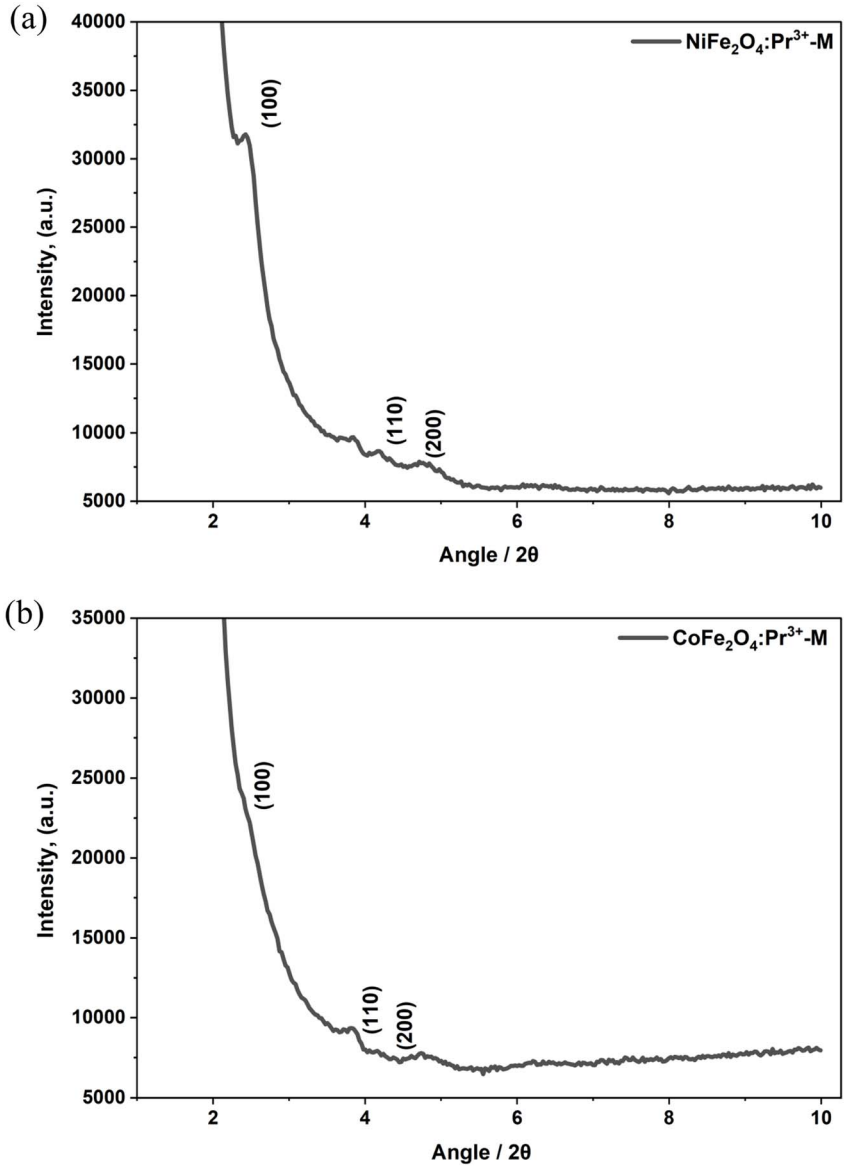


Fig. 3 (a) XRD pattern of $NiFe_2O_4$:$Pr^{3+}$–M. (b) XRD pattern of $CoFe_2O_4$:$Pr^{3+}$–M.

Low-angle XRD analysis was employed to evaluate the preservation of the mesoporous structure, and the corresponding diffraction pattern is shown in Fig. 3(a). The low-angle XRD pattern exhibits a distinct (100) reflection at approximately $2\theta \approx 2°–2.5°$, accompanied by weaker (110) and (200) reflections, which are characteristic of the hexagonally ordered mesoporous structure of MCM-41.[28] The presence of the (100) peak confirms that the mesostructural framework is retained after nanoparticle incorporation. However, the reduced intensity and partial disappearance of higher-order reflections indicate a decrease in long-range ordering, likely due to the pore filling and structural distortion induced by the embedded nanoparticles.

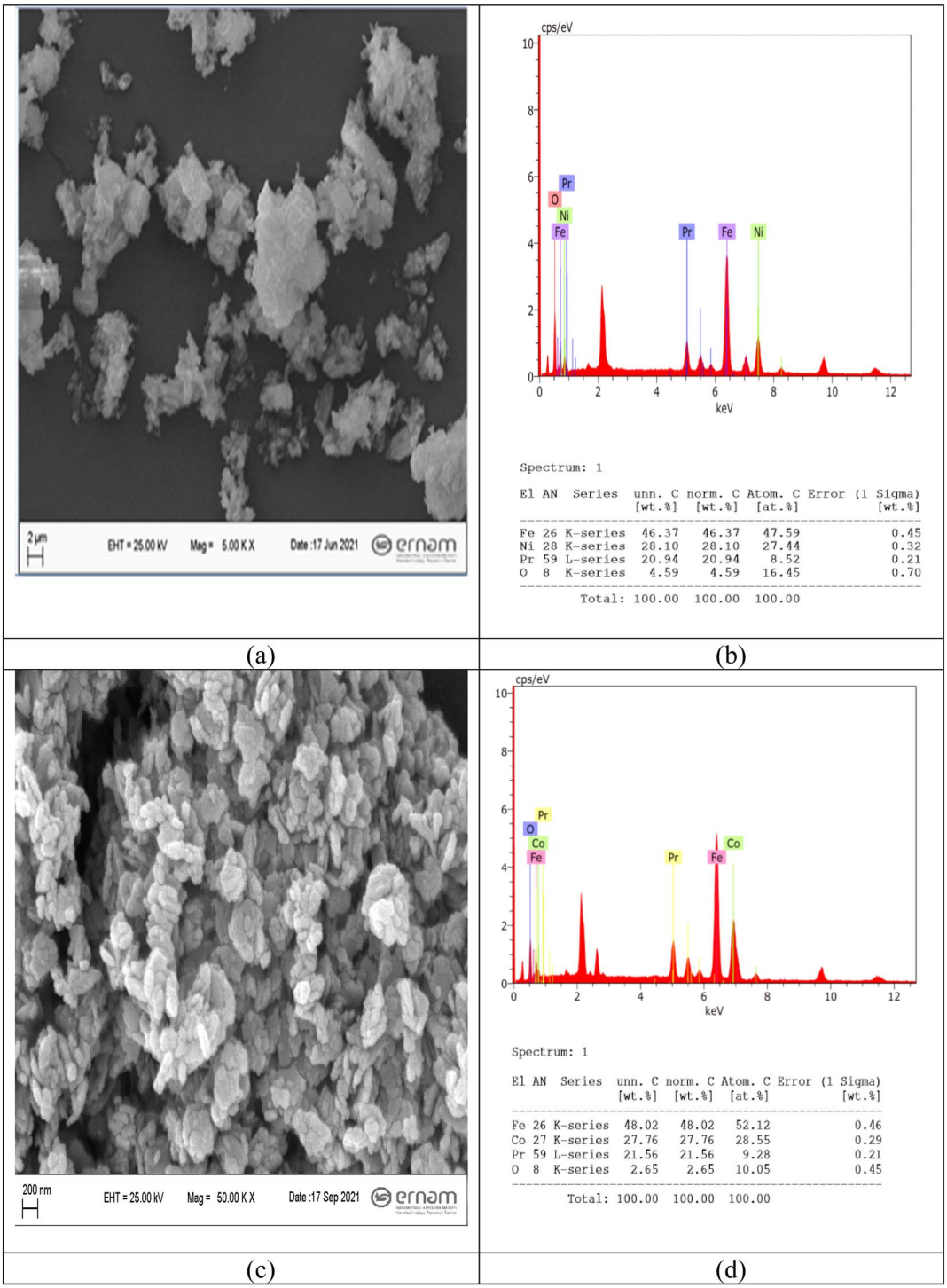


Fig. 4 SEM and EDX analysis of $NiFe_2O_4$:$Pr^{3+}$ and $CoFe_2O_4$:$Pr^{3+}$. (a) SEM image of $NiFe_2O_4$:$Pr^{3+}$. (b) EDX analysis of $NiFe_2O_4$:$Pr^{3+}$. (c) SEM image of $CoFe_2O_4$:$Pr^{3+}$. (d) EDX analysis of $CoFe_2O_4$:$Pr^{3+}$.

The XRD patterns of $CoFe_2O_4$:$Pr^{3+}$ (CoF:$Pr^{3+}$) and $CoFe_2O_4$:-$Pr^{3+}$–MCM-41 (CoF:$Pr^{3+}$–M) are shown in Fig. 2(b). Both samples exhibit the characteristic diffraction peaks of the spinel $CoFe_2O_4$ phase, matching the standard reflections reported in JCPDS card no. 22-1086.[29] The prominent peaks indexed to the (220), (311), (400), (422), (511), and (440) planes confirm that the

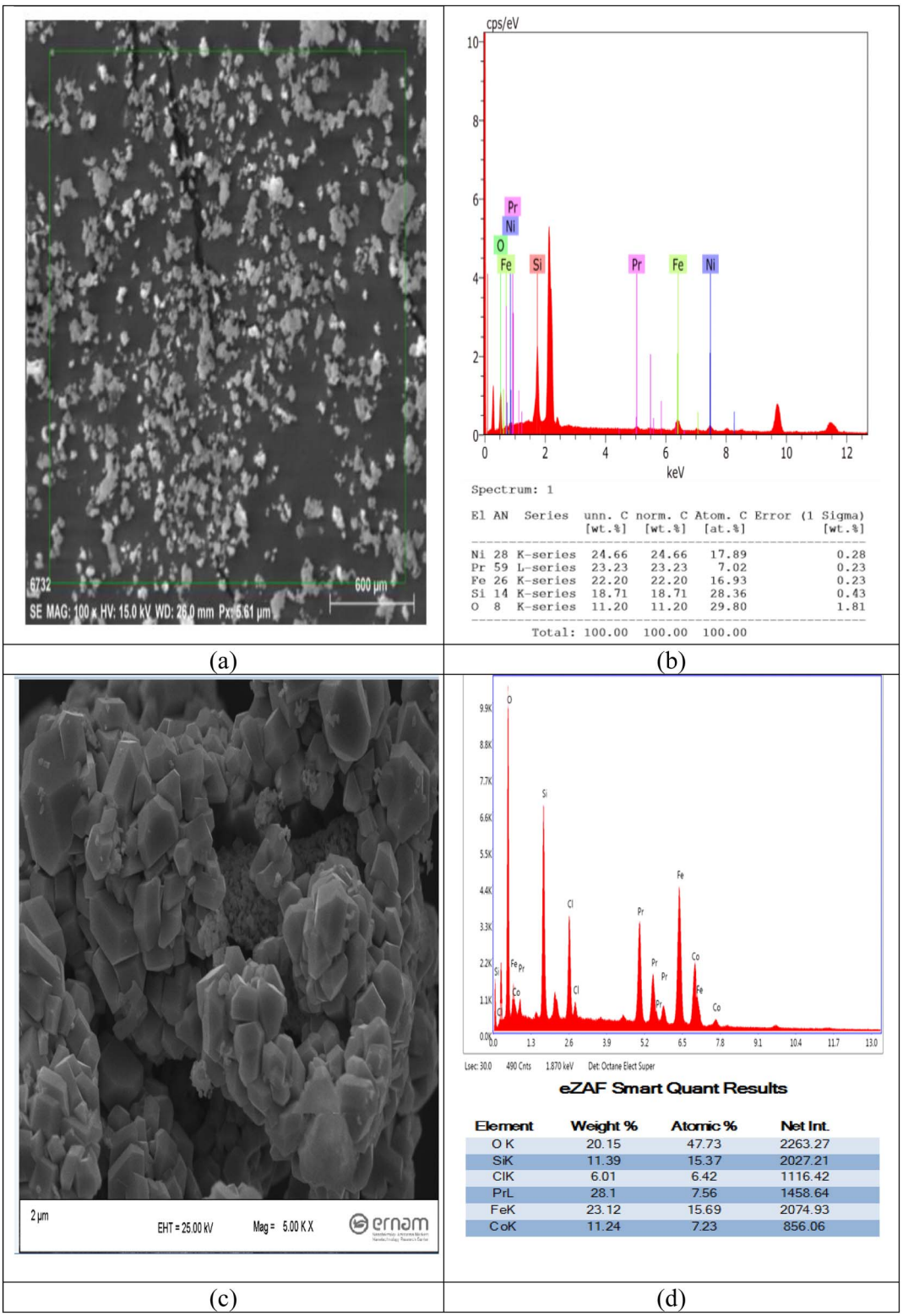


Fig. 5 SEM and EDX analysis of $NiFe_2O_4$:$Pr^{3+}$–MCM-41 and $CoFe_2O_4$:$Pr^{3+}$–MCM-41. (a) SEM image of $NiFe_2O_4$:$Pr^{3+}$–MCM-41. (b) EDX analysis of $NiFe_2O_4$:$Pr^{3+}$–MCM-41. (c) SEM image of $CoFe_2O_4$:$Pr^{3+}$–MCM-41. (d) EDX analysis of $CoFe_2O_4$:$Pr^{3+}$–MCM-41.

spinel structure is formed in both the free powder sample (CoF:$Pr^{3+}$) and the MCM-41-supported sample (CoF:$Pr^{3+}$–M). In addition to the spinel reflections, both samples contain secondary peaks attributed to $\alpha$-$Fe_2O_3$, FeO, and $Pr_2O_3$, indicating the formation of a multi-phase system rather than a single-phase Pr-doped $CoFe_2O_4$ spinel. The presence of these identical impurity phases in both samples suggests that the multi-phase character originates from the high $Pr^{3+}$ content, which exceeds the structural tolerance of the spinel lattice. The large ionic radius of $Pr^{3+}$ restricts its incorporation into the octahedral sites, causing excess Pr to segregate into Pr-oxide phases while promoting Fe-oxide formation due to changes in the Fe redox balance.

For the CoF:$Pr^{3+}$–M sample, which contains partially Pr-doped CoF:$Pr^{3+}$ nanoparticles incorporated into the mesoporous channels of MCM-41 *via* a suspension-impregnation route, the overall diffraction intensity is lower compared to that for the free nanoparticle sample. This reduction can be attributed to the high dispersion of the nanoparticles within the silica framework and the contribution of the broad amorphous hump around $2\theta \approx 23°$, which is characteristic of the disordered silica walls of MCM-41. The appearance of this amorphous background confirms that the MCM-41 structure is preserved during the incorporation process. Despite this, the impurity peaks remain clearly visible, demonstrating that the support does not alter the fundamental phase composition—both samples consistently exhibit $CoFe_2O_4$:$Pr^{3+}$, together with $Pr_2O_3$ and Fe-oxide phases. These results suggest that $Pr^{3+}$ incorporation occurs only partially within the spinel lattice, while excess Pr segregates into secondary phases, leading to a multiphase system rather than a single-phase fully substituted structure.

The low-angle XRD pattern of the CoF:$Pr^{3+}$–M (Fig. 3(b)) exhibits a prominent diffraction peak at $2\theta \approx 2°$–$2.5°$, corresponding to the (100) plane of the hexagonally ordered mesoporous structure of MCM-41. This observation confirms that the fundamental mesostructural framework is retained following the incorporation of $CoFe_2O_4$:$Pr^{3+}$ nanoparticles. In addition, weak and broadened reflections corresponding to the (110) and (200) planes are observed at higher angles, indicating a partial loss of long-range ordering. This reduction in structural periodicity can be attributed to the confinement of ferrite nanoparticles within the mesoporous channels, leading to pore filling and slight distortion of the silica framework. Overall, the results demonstrate that while the ordered mesoporous architecture is preserved, its structural regularity is partially diminished upon nanoparticle incorporation.

The SEM images of the unmodified Ni/CoF:$Pr^{3+}$ are presented in Fig. 4(a)–(d). As shown in Fig. 4(a) and (c), the NiF:$Pr^{3+}$ and CoF:$Pr^{3+}$ particles have a spherical shape with a uniform size distribution. The EDX spectra of the NiFe:$Pr^{3+}$ and CoF:$Pr^{3+}$ nanocomposites are given in Fig. 4(b) and (d), respectively. In Fig. 4(b), the peaks for Fe, Ni, Pr, and O can be observed in the spectrum of NiF:$Pr^{3+}$, and as expected in Fig. 4(d), the peaks for Fe, Co, Pr, and O can be observed in the spectrum of the CoF:$Pr^{3+}$ nanocomposite.

The SEM images of the unmodified Ni/CoF:$Pr^{3+}$–M are presented in Fig. 5(a) and (c). As can be seen in Fig. 5(a) and (c), the NiF:$Pr^{3+}$–M and CoF:$Pr^{3+}$–M particles have a spherical shape with a uniform size distribution. The EDX spectra of the Ni/CoF:$Pr^{3+}$–M nanocomposites are given in Fig. 5(a) and (c). As can be seen in Fig. 5(b), the peaks for Fe, Ni, Pr, Si, and O are observed in the spectrum of NiF:$Pr^{3+}$–M, and as expected in Fig. 5(d), the peaks for Fe, Co, Pr, Si, and O are observed in the spectrum of the CoF:$Pr^{3+}$–M nanocomposite.

The SEM images of the Ni/CoF:$Pr^{3+}$–M@PVDF nanofiber membranes are given in Fig. 6. It was observed that thinner and more uniform nanofibers were obtained using a 1 : 1 DMSO : acetone solution.

To further evaluate the mesoporous characteristics and structural integrity of the materials, nitrogen adsorption–desorption measurements (BET) were performed. NiF:$Pr^{3+}$–M exhibits a typical type-IV isotherm with a hysteresis loop, characteristic of mesoporous materials.[30] The corresponding nitrogen adsorption–desorption isotherms are presented in Fig. 7(a). The BET surface area was determined to be 406.5 $m^2$ $g^{-1}$, which is lower than that of the pristine MCM-41.[31] This reduction indicates the partial occupation of mesoporous channels by nanoparticles. The BJH pore-size distribution shows average pore diameters of 2.42 nm (adsorption) and 2.65 nm (desorption), which fall within the characteristic pore-size range of MCM-41 (2–4 nm). This confirms that the mesoporous framework is preserved despite nanoparticle incorporation. The small difference between adsorption and desorption values suggests minor pore distortion and limited pore blocking.

The nitrogen adsorption–desorption isotherms of CoF:$Pr^{3+}$–M are presented in Fig. 7(b). CoF:$Pr^{3+}$–M similarly exhibits a type-IV isotherm, with a BET surface area of 431.8 $m^2$ $g^{-1}$, indicating a slightly higher accessible surface area compared to that for the Ni-based system. The BJH pore diameters were determined as 2.41 nm (adsorption) and 4.40 nm (desorption). While the adsorption value remains consistent with that for MCM-41, the significantly higher desorption value indicates pronounced hysteresis effects. The deviation between adsorption and desorption branches suggests the presence of pore

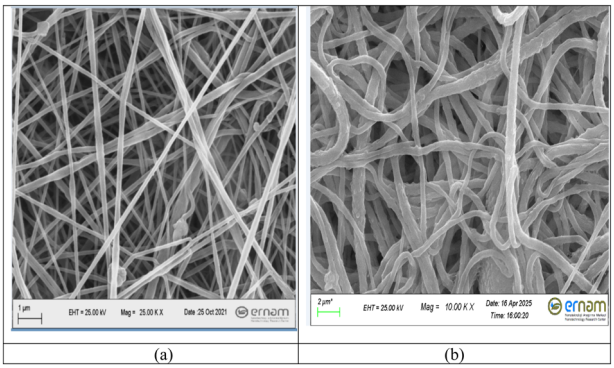


Fig. 6 SEM images of the electrospun nanofiber membranes (a) NiF/M@PVDF/BN and (b) CF/M@PVDF/BN.

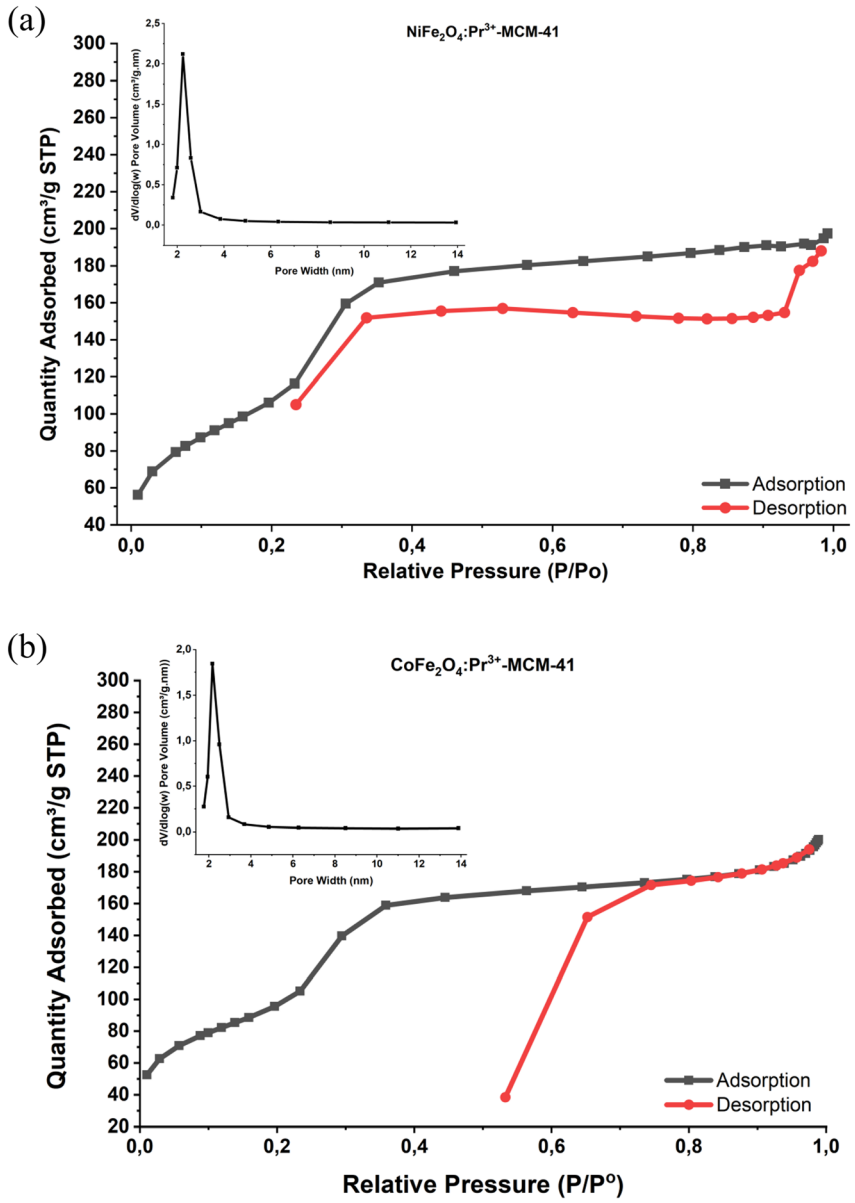


Fig. 7 (a) $N_2$ adsorption–desorption isotherms and pore-size distribution curves of $NiFe_2O_4$:$Pr^{3+}$–MCM-41. (b) $N_2$ adsorption–desorption isotherms and pore-size distribution curves of $CoFe_2O_4$:$Pr^{3+}$–MCM-41.

blocking and ink-bottle-type pore structures, which are commonly observed in nanoparticle-loaded mesoporous systems.[32] This behavior reflects partial pore filling and structural distortion, rather than the collapse of the mesoporous framework. Overall, the combination of the reduced surface area and preserved pore diameter provides strong evidence that the nanoparticles are successfully incorporated within the mesoporous channels rather than merely deposited on the external surface. The preservation of mesoporosity, combined with successful nanoparticle incorporation, results in a synergistic structure that enhances adsorption efficiency while maintaining magnetic separability. The reproducibility of extraction performance further confirms that the structural modifications do not adversely affect functional stability.

The FT-IR spectra of NiF:$Pr^{3+}$/NiF:$Pr^{3+}$–M and CoF:$Pr^{3+}$/CoF:$Pr^{3+}$–M are presented in Fig. 8(a) and (b), respectively. As can be seen in Fig. 8(a), the NiF:$Pr^{3+}$–M nanocomposites show characteristic absorption bands, indicating the presence of ferrite-related vibrational modes together with the silica framework. Specifically, the spectrum of bare NiF:$Pr^{3+}$ displays prominent bands at approximately 3420 $cm^{-1}$ (broad O–H stretching from surface hydroxyl groups or adsorbed water), 1630 $cm^{-1}$ (H–O–H bending vibration of water molecules), 590 $cm^{-1}$ (tetrahedral Fe–O stretching vibration), and 410 $cm^{-1}$ (octahedral Ni–O stretching vibration).[33] These bands are indicative of the inverse spinel structure, where $Fe^{3+}$ ions predominantly occupy tetrahedral sites and $Ni^{2+}$/$Pr^{3+}$ ions may partially substitute into octahedral sites, although the XRD

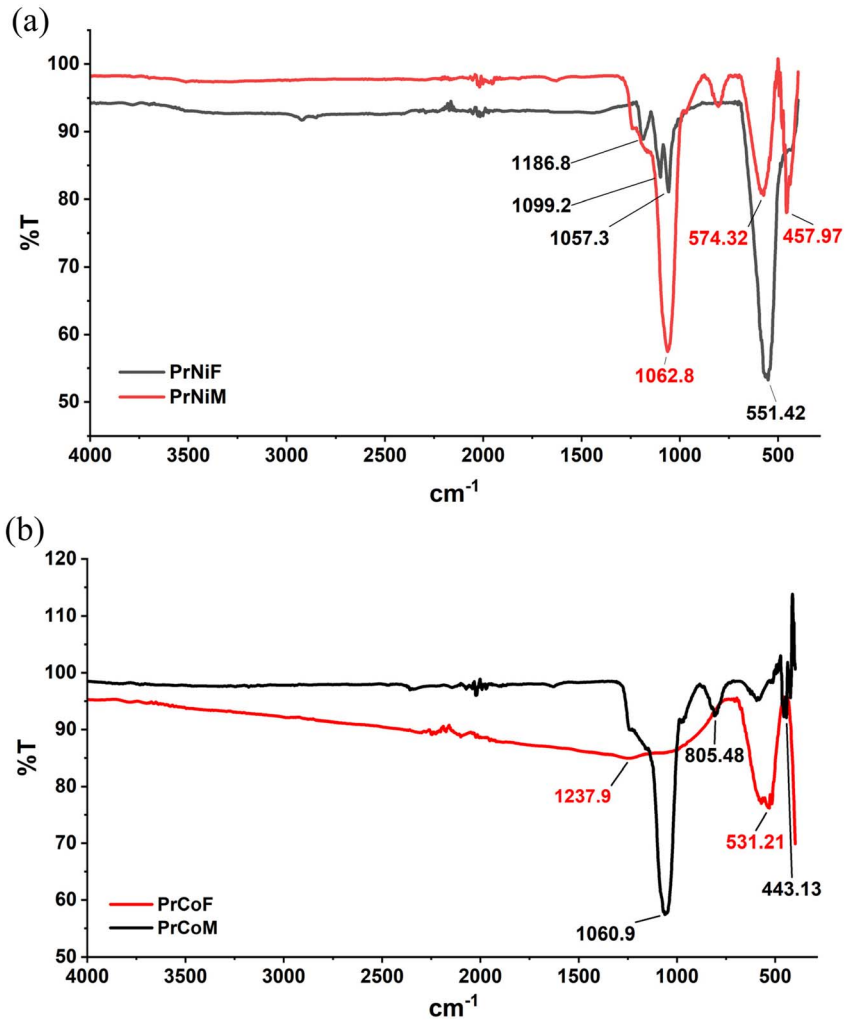


Fig. 8 (a) FTIR spectra of $NiFe_2O_4$:$Pr^{3+}$(F) and $NiFe_2O_4$:$Pr^{3+}$–MCM-41 (M). (b) FTIR spectra of $CoFe_2O_4$:$Pr^{3+}$(F) and $CoFe_2O_4$:$Pr^{3+}$–MCM-41 (M).

results indicate that complete incorporation is not achieved. The incorporation of $Pr^{3+}$ causes a slight broadening and downshift (by ~5–10 $cm^{-1}$) in the octahedral band compared to that of the undoped $NiFe_2O_4$, attributed to lattice distortions due to the larger ionic radius of $Pr^{3+}$ (0.99 Å) *versus* $Fe^{3+}$ (0.645 Å), leading to modified bond strengths and vibrational frequencies.[34,35] Upon compositing with MCM-41, additional bands emerge at 1080 $cm^{-1}$ (asymmetric Si–O–Si stretching), 800 $cm^{-1}$ (symmetric Si–O–Si stretching), and 460 $cm^{-1}$ (Si–O bending vibration), which are hallmark features of the siliceous MCM-41 matrix.[34] The Si–OH stretching band, typically strong at ~960–970 $cm^{-1}$ for the pure MCM-41, appears weakened and shifted to ~950 $cm^{-1}$ in the composite, suggesting hydrogen bonding or covalent interactions between the silica surface hydroxyls and the ferrite nanoparticles, which could facilitate better dispersion and prevent agglomeration during electrospinning. This interfacial interaction may enhance composite stability; however, no clearly distinguishable additional bands are observed, and the absence of resolved Pr–O vibrations in the 500–600 $cm^{-1}$ region cannot be taken as evidence of complete incorporation of $Pr^{3+}$ into the ferrite lattice, as overlapping metal–oxygen vibrations may mask contributions from Pr-containing secondary phases, consistent with the XRD results.

The overall transmittance decreases in the composite spectrum, reflecting increased scattering from the heterogeneous structure, a common observation in nanoparticle-silica hybrids. Similarly, in Fig. 8(b), the CoF:$Pr^{3+}$–M nanocomposites exhibit analogous features, with bare CoF:$Pr^{3+}$ showing bands at 3440 $cm^{-1}$ (O–H stretch), 1620 $cm^{-1}$ (H–O–H bend), 580 $cm^{-1}$ (tetrahedral Fe–O), and 400 $cm^{-1}$ (octahedral Co–O).[36] $Pr^{3+}$ doping here induces a comparable shift in the octahedral band (to ~390–395 $cm^{-1}$), consistent with the substitution at $Co^{2+}$ sites (ionic radius: 0.745 Å).[34,35] The MCM-41 integration introduces Si–O–Si bands at 1075 $cm^{-1}$ (asym.), 795 $cm^{-1}$ (sym.), and 455 $cm^{-1}$ (bend), with similar weakening of the Si–OH band, indicating effective anchoring of the ferrite onto the silica pores and potentially improving the material's reusability in adsorption cycles.[37] Compared to the Ni-based composite, the Co-based composite shows slightly higher intensity in the M–O bands, possibly due to the more substantial magneto-crystalline anisotropy of Co ferrites. These FTIR results are consistent with the presence of bonds associated with ferrite and silica;

however, it is important to note that the phase composition was more reliably determined by XRD, which indicates a multi-phase structure. The modified surface functional groups (*e.g.*, increased Si–OH availability) improve the binding affinity for heavy metals and organic pollutants, potentially through electrostatic or chelation mechanisms. Overall, the FTIR spectra confirm the presence of ferrite and silica-related vibrational modes and suggest possible lattice distortions due to $Pr^{3+}$ addition. However, consistent with the XRD results, the system should be considered as a multi-phase composite rather than a single-phase Pr-doped spinel.

Also, the thermal stability and structural degradation stages of the synthesized $CoFe_2O_4$:$Pr^{3+}$–MCM-41 nanocomposite were investigated by thermogravimetric analysis (TGA) and differential thermogravimetric analysis (DTG) from room temperature up to 1000 °C (Fig. 9(a)). The overall TGA curve demonstrates that the material exhibits an extremely low total mass loss of only ~3% up to 1000 °C, which clearly confirms the excellent thermal and structural stability of the entirely inorganic oxide and silica-based framework. The thermal profile of the material can be evaluated in four main stages. The minor mass loss (~1%) observed in the first stage, from room temperature to approximately 200 °C, is attributed to the evaporation of the physically adsorbed water molecules on the sample surface and the residual volatile solvents trapped within the MCM-41 pore structure.[38] In the second stage (200 °C–600 °C), the steady and slow mass loss represents the gradual dehydroxylation of the surface silanol (–OH) groups in the MCM-41 framework and the removal of crystalline water. The very limited mass loss in this region verifies that the material was successfully calcined during the synthesis and is free of organic impurities.[38] In the third stage (750 °C–900 °C), a specific mass gain in the TGA curve and a corresponding distinct positive peak in the DTG curve (approximately +5 μg $min^{-1}$) were detected. This phenomenon indicates the occurrence of partial oxidation processes due to oxygen uptake by the transition metals (specifically cobalt or iron ions) in the spinel ferrite structure at high temperatures under atmospheric conditions.[39] Finally, the sharp mass loss observed above 900 °C can be associated with the thermal degradation (structural collapse) of the ordered mesoporous silica network or high-temperature reduction reactions in the ferrite phase.[40] All these thermal findings indicate that the $CoFe_2O_4$:$Pr^{3+}$–MCM-41 material possesses more than enough structural integrity and high stability for adsorption applications, such as wastewater treatment, which are typically carried out in aqueous environments at room temperature.

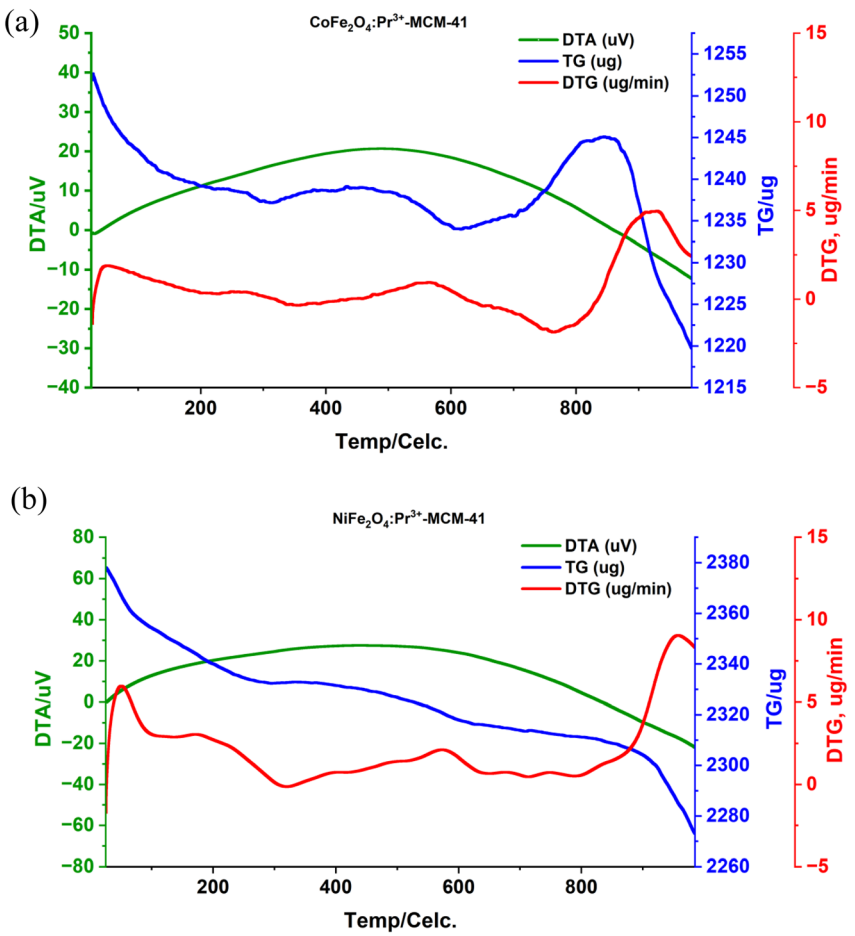


Fig. 9 (a) TGA/DTA curves of the $CoFe_2O_4$:$Pr^{3+}$–MCM-41 nanocomposite. (b) TGA/DTA curves of the $NiFe_2O_4$:$Pr^{3+}$–MCM-41 nanocomposite.

Similarly, the thermal degradation profile of the synthesized $NiFe_2O_4$:$Pr^{3+}$–MCM-41 nanocomposite was evaluated under identical conditions (Fig. 9(b)). The overall TGA curve indicates a total mass loss of only ~4.8% up to 1000 °C, confirming the highly stable nature of this inorganic composite. The thermal decomposition occurs in three distinct stages. In the first stage (from room temperature to 200 °C), an initial mass loss of ~1.7% is observed, which corresponds to the elimination of the physically adsorbed water and residual volatile solvents trapped inside the mesopores.[38] The second stage (200 °C to 800 °C) is characterized by a very slow and gradual mass loss (~1.2%), which is attributed to the continuous dehydroxylation of the surface silanol (–OH) groups of the MCM-41 framework and the loss of structurally bound water.[38] Unlike the cobalt-based nanocomposite, the $NiFe_2O_4$:$Pr^{3+}$–MCM-41 sample does not exhibit a distinct mass gain related to high-temperature oxygen uptake, reflecting the different oxidation kinetics of the nickel-based spinel lattice. In the final stage (above 850 °C), a sharp mass loss (~1.9%) accompanied by a prominent DTG peak is recorded. This sudden mass loss is ascribed to the ultimate thermal degradation and structural collapse of the ordered mesoporous silica network.[30] Collectively, the TGA results for both Ni- and Co-based nanocomposites prove that the bare powder materials possess extraordinary thermal stability and structural integrity, rendering them highly durable prior to their integration into the final polymeric electrospun membranes.

### 3.2. Selection of the optimal pH

The pH of the aqueous solution is a significant variable that controls the adsorption of Cr, Pb, Ni, and As on NiF:$Pr^{3+}$–M@PVDF and Al, Co, Cd, and Hg on CoF:$Pr^{3+}$–M@PVDF for wastewater samples. Therefore, the effect of pH on the adsorption of Cr, Pb, Ni, As, Al, Co, Cd, and Hg was studied in the pH range of 1–10 using 0.1 mol $L^{-1}$ $HNO_3$/NaOH solutions (see Table 2). It can be observed that the adsorption of Cr, Pb, Ni, and As decreases with increasing pH, whereas the adsorption of Al, Co, Cd, and Hg increases with increasing pH. At high pH values, the recovery values decrease, probably due to the precipitation of hydroxides. Therefore, the optimum pH values were chosen separately for each nanofiber membrane: pH 2 for NiF:$Pr^{3+}$–M@PVDF and pH 4 for CoF:$Pr^{3+}$–M@PVDF.

### 3.3. Zeta potential measurements

The zeta potentials of the Ni/CoF:$Pr^{3+}$–M@PVDF nanofiber membranes were measured in a pH range of 1–10. As seen in Fig. 10, the Ni/CoF:$Pr^{3+}$–M@PVDF nanofiber membranes displayed a positive surface potential between pH 1 and 5, while after the adsorption of Cr, Pb, Ni, As, Al, Co, Cd, and Hg, the Ni/CoF:$Pr^{3+}$–M@PVDF nanofiber membranes indicated positive zeta potentials at pH 2 and 4. This result indicates that the adsorption of Cr, Pb, Ni, As, Al, Co, Cd, and Hg elements onto the particles of nanofiber membranes may have taken place by electrostatic interactions between Cr, Pb, Ni, As, Al, Co, Cd, and Hg and the Ni/CoF:$Pr^{3+}$–M@PVDF nanofiber membranes.

### 3.4. Effect of contact time for adsorption and elution

The effect of contact times for the adsorption and elution of Cr, Pb, Ni, and As on NiF:$Pr^{3+}$–M@PVDF and Al, Co, Cd, and Hg on CoF:$Pr^{3+}$–M@PVDF was investigated. The effect of contact times for the adsorption and elution of analytes was tested using model solutions of 25 mL of the wastewater samples with 25 mg of NiF:$Pr^{3+}$–M@PVDF and 100 mg CoF:$Pr^{3+}$–M@PVDF at pH 2 and pH 4, respectively, for 0, 1, 2, 3, 5, and 10 min. By increasing the contact times, the concentrations of analytes increased and remained stable thereafter. The adsorption and elution of analyte ions reached equilibrium within 3 minutes. Therefore, we selected a contact time of 3 min for both adsorption and elution in all subsequent experiments.

### 3.5. Effect of eluent type, concentration, and volume

Concentrations of strong acid solutions, including HCl and $HNO_3$, were tested for the elution of Cr, Pb, Ni, As, Al, Co, Cd, and Hg from the Ni/CoF:$Pr^{3+}$–M@PVDF nanofiber membranes. Aliquots of 5 mL of 0.5, 1, 2, and 3 mol $L^{-1}$ of HCl and $HNO_3$ were used. The results indicated that the maximum recovery

Table 2 Effect of pH ($n = 3$, μg $L^{-1}$)

| Element concentration ($\bar{X} \pm s$) | | | | | | | | |
|---|---|---|---|---|---|---|---|---|
| | NiF:$Pr^{3+}$–M@PVDF | | | | CoF:$Pr^{3+}$–M@PVDF | | | |
| pH | Cr | Pb | Ni | As | Al | Co | Cd | Hg |
| 1 | 6.57 ± 0.12 | 9.82 ± 0.23 | 106 ± 7 | 0.112 ± 0.01 | 5.80 ± 0.15 | 20.4 ± 0.9 | 0.538 ± 0.009 | 1.250 ± 0.01 |
| 2 | 7.16 ± 0.14 | 9.92 ± 0.25 | 108 ± 6 | 0.122 ± 0.01 | 6.02 ± 0.14 | 21.9 ± 1.1 | 0.545 ± 0.01 | 1.256 ± 0.01 |
| 3 | 7.04 ± 0.12 | 9.77 ± 0.34 | 104 ± 8 | 0.119 ± 0.02 | 6.33 ± 0.14 | 22.9 ± 0.8 | 0.611 ± 0.008 | 1.289 ± 0.014 |
| 4 | 6.68 ± 0.18 | 9.11 ± 0.41 | 100 ± 6 | 0.091 ± 0.01 | 6.90 ± 0.19 | 24.6 ± 0.9 | 0.678 ± 0.01 | 1.382 ± 0.01 |
| 5 | 5.345 ± 0.10 | 8.92 ± 0.55 | 92 ± 6 | 0.085 ± 0.01 | 6.71 ± 0.26 | 24.2 ± 1.2 | 0.527 ± 0.01 | 1.267 ± 0.11 |
| 6 | 4.312 ± 0.11 | 8.83 ± 0.46 | 78 ± 5 | 0.067 ± 0.01 | 5.81 ± 1.12 | 21.1 ± 1.4 | 0.311 ± 0.01 | 1.248 ± 0.017 |
| 7 | 2.345 ± 0.17 | 6.21 ± 0.51 | 35 ± 6 | — | 5.12 ± 1.27 | 17.1 ± 1.3 | — | 1.111 ± 0.13 |
| 8 | —[a] | — | — | — | — | 12.2 ± 1.3 | — | — |
| 9 | — | — | — | — | — | — | — | — |
| 10 | — | — | — | — | — | — | — | — |

[a] Below the detection limit.

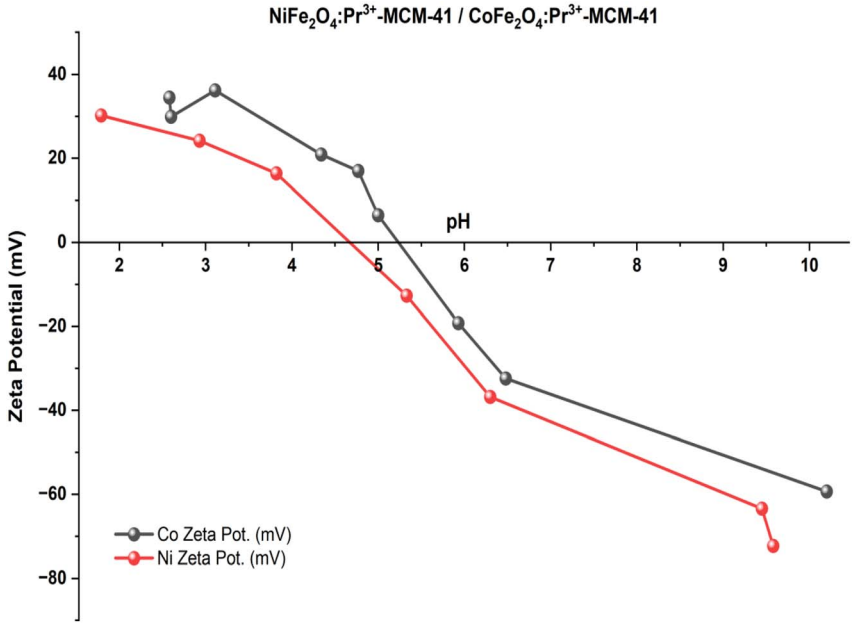


Fig. 10 Zeta potentials of the Ni/CoF:$Pr^{3+}$–M@PVDF nanofiber membranes.

values for Cr, Pb, Ni, and As were obtained with 2 mol $L^{-1}$ $HNO_3$ (1 mL), while 2 mol $L^{-1}$ HCl (1 mL) was chosen as the optimum eluent for Al, Co, Cd, and Hg in the subsequent experiments.

The effect of the eluent volume on the quantitative elution of Cr, Pb, Ni, As, Al, Co, Cd, and Hg was investigated using 1, 2, 3, 4, and 5 mL of 2 mol $L^{-1}$ $HNO_3$ and 2 mol $L^{-1}$ HCl. The maximum recovery values for Cr, Pb, Ni, As, Al, Co, Cd, and Hg were obtained using 1 mL of the 2 mol $L^{-1}$ $HNO_3$ and 1 mL of the 2 mol $L^{-1}$ HCl solution. There was no increase in the maximum concentrations with increasing the eluent volume. Thus, an eluent volume of 1 mL was selected as the optimum to obtain a high pre-concentration factor for subsequent experiments.

### 3.6. Effect of sample volume

The effect of sample volume was investigated using 25, 50, 100, 150, 200, 250, and 500 mL of the wastewater samples. Then, adsorption and elution were performed under the optimum conditions (pH 2 and pH 4; contact time, 3 min; 1 mL of eluent), as described in Section 2.6. The concentrations of analytes were found to be optimal for volumes ranging from 25 to 250 mL. Volumes higher than 250 mL resulted in a decrease in the concentration of analytes. Therefore, a sample volume of 250 mL was selected as the optimum, and the pre-concentration factor of the method was found to be 250.

### 3.7. Reusability of the adsorbents

The reusability of the adsorbents is expected to improve their utilization efficiency and reduce the analysis costs.[41,42] The reusability of the NiF:$Pr^{3+}$–M@PVDF and CoF:$Pr^{3+}$–M@PVDF nanofiber membranes (life-time) was investigated using the proposed procedure. Before each cycle, the nanofiber membranes were rinsed with ultra-pure water. It was found that the life-time was exceptionally long because no loss was observed in the recovery rates throughout the study. The results indicated that the nanofiber membranes remained stable up to 60 cycles without a noticeable decrease in the concentrations of the analytes. Therefore, the $NiFe_2O_4$:$Pr^{3+}$–MCM-41 and $CoFe_2O_4$:$Pr^{3+}$–MCM-41 nanofiber membranes show better reusability and stability towards Cr, Pb, Ni, As, Al, Co, Cd, and Hg.

### 3.8. Effect of interferences

The effect of sample matrix components on the recovery of Cr, Pb, Ni, As, Al, Co, Cd, and Hg analytes in wastewater samples was investigated. NaCl, KCl, $Mg(NO_3)_2$, $Ca(NO_3)_2$, $Cu(NO_3)_2$, $Fe(NO_3)_3$, $Fe(NO_3)_2$, $Zn(NO_3)_2$, $Mn(NO_3)_2$, $Na_2SO_4$, and $Na_3PO_4$, within the range of 25–10.000 mg $L^{-1}$, were added to 25 mL wastewater sample solutions. After that, the developed magnetic d-μSPE method was applied. The recovery values of these ions were observed to be ≥95% for 10.000 mg $L^{-1}$ of Na(I), K(I) and Mg(II); 20.000 mg $L^{-1}$ of Ca(II); 25 mg $L^{-1}$ of Cu(II), Fe(III), Fe(II), Zn(II) and Mn(II); and 2500 mg $L^{-1}$ of $SO_4^{2-}$ and $PO_4^{3-}$. The results indicate that the developed method is suitable for the accurate and selective determination of Cr, Pb, Ni, As, Al, Co, Cd, and Hg in wastewater samples.

### 3.9. Adsorption capacity

The adsorption capacity of the Ni/CoF:$Pr^{3+}$–M@PVDF nanofiber membranes is an important parameter, and it was studied under the optimum conditions given in Section 2.6. The investigation was conducted in five replicates. For this purpose, first, 25 mg of the NiF:$Pr^{3+}$–M@PVDF was suspended in a 25 mL aqueous solution containing 10 mg $L^{-1}$ of Cr(III), Pb(II), Ni(II), and As(III) at pH 2 by vortexing for 3 min. Then, the NiF:$Pr^{3+}$–M@PVDF material was separated from the solution by centrifuging at 4000 rpm for 1 min. The concentrations of Cr, Pb, Ni,

and As ions in the remaining solution were determined by ICP-MS after 100-fold dilution.

Second, the adsorption capacity was investigated for the CoF:$Pr^{3+}$–M@PVDF nanofiber membranes. 100 mg of CoF:$Pr^{3+}$–M@PVDF was suspended in a 25 mL aqueous solution containing 10 mg $L^{-1}$ of Al(III), Co(II), Cd(II), and Hg(II) at pH 4 by vortexing for 3 min. Then, the CoF:$Pr^{3+}$–M@PVDF material was separated from the solution by centrifuging at 4000 rpm for 1 min. The concentrations of Al, Co, Cd, and Hg ions in the remaining solution were determined by ICP-MS after 100-fold dilution.

The adsorption capacity of the Ni/CoF:$Pr^{3+}$–M@PVDF nanofiber membranes was calculated by the equation: $q = \frac{V(C_o - C_e)}{W}$.[43]

In this equation, $q$, $V$, $C_o$, $C_e$, and $W$ indicate the adsorption capacity (mg $g^{-1}$); volume (L); initial concentration of Cr(III), Pb(II), Ni(II), As(III), Al(III), Co(II), Cd(II), or Hg(II) (mg $L^{-1}$); equilibrium concentration of Cr(III), Pb(II), Ni(II), As(III), Al(III), Co(II), Cd(II), or Hg(II) (mg $L^{-1}$); and the adsorbent mass (g), respectively. The $q$ (adsorption capacity) values for the elements optimized for NiF:$Pr^{3+}$–M@PVDF and CoF:$Pr^{3+}$–M@PVDF were found to be 14.9 mg $g^{-1}$ for Cr, 12.3 mg $g^{-1}$ for Pb, 10.8 mg $g^{-1}$ for Ni, 8.67 mg $g^{-1}$ for As, 32.9 mg $g^{-1}$ for Al, 13.4 mg $g^{-1}$ for Co, 28.4 mg $g^{-1}$ for Cd and 23.5 mg $g^{-1}$ for Hg.

### 3.10. *E. coli* enumeration

*E. coli* colony counts were evaluated over three weeks in influent wastewater samples (Table 3). The results demonstrated that both nanofiber membrane materials substantially reduced the *E. coli* load in influent wastewater. In the control samples, bacterial concentrations remained consistently high throughout the three weeks, ranging from 21.6 to 30.4 CFU $mL^{-1}$. In contrast, the influent samples treated with NiF:$Pr^{3+}$–M@PVDF showed a marked reduction, with *E. coli* levels decreasing to 0–0.3 CFU $mL^{-1}$, and complete inhibition (0 CFU $mL^{-1}$) was observed in the first and third weeks. CoF:$Pr^{3+}$–M@PVDF exhibited even stronger antimicrobial performance, achieving complete elimination (0 CFU $mL^{-1}$) in all influent samples across all three weeks.

The ability of both nanomaterials to maintain similar levels of antimicrobial activity over the experimental period indicates high stability and sustained efficacy, even under the high microbial load characteristic of influent wastewater. Compared to the consistently elevated counts in the control group, the dramatic reduction achieved by the nanocomposites highlights their strong and reliable antibacterial action.

To better interpret this strong antibacterial performance, a plausible removal mechanism is proposed. The complete removal of *E. coli* is most plausibly governed by a synergistic mechanism involving surface-mediated oxidative stress and physical interactions rather than metal-ion toxicity.[43–47] Given the structural stability of the nanocomposites over repeated cycles, ion leaching is expected to be minimal. The ferrite phase ($NiFe_2O_4$ and $CoFe_2O_4$) is known to promote the generation of reactive oxygen species (ROS) through surface redox processes, leading to oxidative damage of bacterial membranes, proteins, and nucleic acids.[43–47] In parallel, the electrospun nanofiber architecture provides high surface area and nanoscale roughness, facilitating direct physical contact that can contribute to bacterial membrane disruption.[48] Additionally, the porous MCM-41 framework can facilitate bacterial adsorption and immobilization on the surface, which may increase local exposure to ROS and surface interactions, thereby contributing to the reduction of the *E. coli* levels.[48,49]

### 3.11. Organic pollutant removal

The organic matter removal behavior of the Ni/CoF:$Pr^{3+}$–M@PVDF nanofiber membranes was evaluated based on COD values for both untreated (influent) and treated (effluent) wastewater samples at dosages of 25 mg and 100 mg and contact times of 50 and 20 minutes, respectively. Samples were obtained in different weeks, allowing for the evaluation of the effect of time-dependent variability of the actual wastewater matrix (*e.g.*, organic load and dissolved/particulate matter distribution) on system performance. The obtained COD results and the corresponding removal efficiencies are presented in Table 4. The COD values in the untreated wastewater ranged from 289 to 385 mg $L^{-1}$, while in the treated wastewater, these values ranged from 30 to 36 mg $L^{-1}$. The COD removal performance of the facility was calculated to be in the range of 88–91%, depending on the influent concentration.

The membranes were evaluated under operational conditions determined by considering their structural properties and preliminary experimental observations. Therefore, the obtained COD removal results were evaluated not for directly comparing the intrinsic performances of the two materials, but to reveal the behavior observed under specific conditions and within the actual wastewater matrix. For untreated wastewater, COD removal values ranging from 8%–55% were obtained with the NiF:$Pr^{3+}$–M@PVDF nanofiber membranes and up to 76% under

Table 3 *E. coli* colony counts in wastewater samples (CFU: colony forming units)

| | Sample type | Filtered volume | 1st week | 2nd week | 3rd week |
|---|---|---|---|---|---|
| Control | Influent | 10 mL | 21.6 CFU $mL^{-1}$ | 29.2 CFU $mL^{-1}$ | 27.0 CFU $mL^{-1}$ |
| | Influent | 20 mL | 24.8 CFU $mL^{-1}$ | 30.4 CFU $mL^{-1}$ | 21.5 CFU $mL^{-1}$ |
| NiF:$Pr^{3+}$–M@PVDF | Influent | 10 mL | 0 | 0.30 CFU $mL^{-1}$ | 0 |
| | Influent | 20 mL | 0 | 0.25 CFU $mL^{-1}$ | 0 |
| CoF:$Pr^{3+}$–M@PVDF | Influent | 10 mL | 0 | 0 | 0 |
| | Influent | 20 mL | 0 | 0 | 0 |

Table 4 COD removal performance of the Ni/CoF:$Pr^{3+}$–M@PVDF nanofiber membranes in treated wastewater and untreated effluent samples

| Nanofiber membrane | Nanofiber dose (mg) | Contact time (min) | Untreated wastewater (mg $L^{-1}$) | Nanofiber-treated wastewater (mg $L^{-1}$) | Removal rate (%) | Treated wastewater (mg $L^{-1}$) | Nanofiber-treated wastewater (mg $L^{-1}$) | Removal rate (%) |
|---|---|---|---|---|---|---|---|---|
| NiF:$Pr^{3+}$–M@PVDF | 25 | 50 | 301 | 278 | **8** | 30 | 32 | −7 |
| NiF:$Pr^{3+}$–M@PVDF | 25 | 50 | 385 | 376 | **2** | 36 | 101 | −181 |
| NiF:$Pr^{3+}$–M@PVDF | 25 | 50 | 289 | 525 | −82 | 36 | 154 | −328 |
| NiF:$Pr^{3+}$–M@PVDF | 25 | 50 | 313 | 141 | **55** | 33 | 43 | −30 |
| CoF:$Pr^{3+}$–M@PVDF | 100 | 20 | 301 | 2563 | −751 | 30 | 28 | **7** |
| CoF:$Pr^{3+}$–M@PVDF | 100 | 20 | 385 | 913 | −137 | 36 | 111 | −208 |
| CoF:$Pr^{3+}$–M@PVDF | 100 | 20 | 289 | 359 | −24 | 36 | 241 | −569 |
| CoF:$Pr^{3+}$–M@PVDF | 100 | 20 | 313 | 76 | **76** | 33 | 43 | −30 |

certain conditions with the CoF:$Pr^{3+}$–M@PVDF nanofiber membranes. These findings indicate that the composite materials can effectively interact with organic compounds under relatively high initial loading conditions, suggesting their potential applicability in a complementary treatment step for untreated wastewater. However, the wide range of the results and the observation of negative removal values in some cases show that the system performance is sensitive not only to material properties but also to variability in the wastewater matrix and operating conditions. When the removal values obtained with the NiF:$Pr^{3+}$–M@PVDF nanofiber membranes at lower dosages are evaluated together with the results observed for the CoF:$Pr^{3+}$–M@PVDF nanofiber membranes at higher dosages and shorter contact times, it is understood that the performance differences vary depending on the experimental conditions and matrix properties. Similarly, it has been widely reported in the literature that process efficiencies in real wastewater systems can vary depending on matrix composition, competitive interactions, and operating parameters. The observed COD removal behaviors of the Ni/CoF:$Pr^{3+}$–M@PVDF nanofiber membranes are consistent with the trends reported in studies where metal complexes were immobilized on MCM-41. Reddy *et al.*[50] reported that the mesoporous structure of MCM-41 facilitates the diffusion of organic molecules and strengthens the surface interactions of metal centers. They demonstrated that transition metal complexes bound to MCM-41 interact strongly with organic molecules, reducing the diffusion limits of the mesoporous silica matrix and significantly enhancing organic matter retention. Similarly, Bahrami *et al.*[51] emphasized that the combined effect of the ferrite core and the mesoporous structure plays a role in organic load reduction. These findings support the possible mechanistic basis of the removal behavior observed in the study.

The electrospun nanofiber structure improves mass-transfer processes by providing a high surface area and multiple active sites. Chen *et al.*[52] and Tang *et al.*[53] showed that functional nanofiber-based membranes exhibit strong diffusion properties against organic pollutants and that surface interactions become more effective when combined with metal oxides or mesoporous composites. In this context, the obtained results are consistent with the behavior of the nanofiber-mesoporous composite systems reported in the literature.

The low removal efficiency observed in the treated wastewater is related to the adsorption processes becoming diffusion-controlled at low organic-matter concentrations. This situation has been widely reported in several studies[54–56] focusing on MCM-41 composites modified with transition metal oxides, where limited access to active sites at low concentration levels can reduce removal efficiency. Furthermore, some studies have indicated that electrospun composites may exhibit limited organic matter release at low concentrations, which can contribute to experimental fluctuations.[52]

Overall, an appreciable COD removal efficiency was observed in the untreated wastewater, which can be associated with the surface chemistry of the ferrite core, the mesoporous structure of MCM-41, and the enhanced mass transfer provided by the electrospun nanofiber structure. In contrast, the relatively low

Table 5 Assessment of the accuracy of the method by the certified reference material, CWW-TMD, in wastewater ($n = 3$)

| | Concentration, $\bar{X} \pm s$ (mg $L^{-1}$) | | | | | |
|---|---|---|---|---|---|---|
| | NiF:$Pr^{3+}$–M@PVDF | | | CoF:$Pr^{3+}$–M@PVDF | | |
| Element | Certified value | Determined value | Recovery (%) | Certified value | Determined value | Recovery (%) |
| Cr | 1.00 | 0.98 ± 0.01 | 98 | 1.00 | 0.99 ± 0.01 | 99 |
| Pb | 1.00 | 0.99 ± 0.04 | 99 | 1.00 | 0.99 ± 0.02 | 99 |
| Ni | 1.00 | 1.01 ± 0.02 | 101 | 1.00 | 1.00 ± 0.03 | 100 |
| As | 0.25 | 0.245 ± 0.01 | 98 | 0.25 | 0.25 ± 0.08 | 100 |
| Al | 1.00 | 0.99 ± 0.05 | 99 | 1.00 | 0.97 ± 0.03 | 97 |
| Co | 1.00 | 0.97 ± 0.04 | 97 | 1.00 | 0.98 ± 0.05 | 98 |
| Cd | 0.25 | 0.250 ± 0.001 | 100 | 0.25 | 0.249 ± 0.007 | 100 |
| Hg | 0.02 | 0.019 ± 0.001 | 95 | 0.02 | 0.019 ± 0.004 | 95 |

Table 6 Analysis results of Cr, Pb, Ni, As, Al, Co, Cd, and Hg in water samples ($n = 3$, μg $L^{-1}$)

| | Wastewater | | | Tap water | | |
|---|---|---|---|---|---|---|
| | Added (μg $L^{-1}$) | Found (μg $L^{-1}$) | $R$ (%) | Added (μg $L^{-1}$) | Found (μg $L^{-1}$) | $R$ (%) |
| Cr | —[a] | — | — | — | — | — |
| | 50 | 48 ± 3[b] | 96 | 50 | 49 | 98 |
| | 100 | 97 ± 5 | 97 | 100 | 99 | 99 |
| Pb | — | 6.55 ± 0.18 | — | — | — | — |
| | 50 | 55 ± 3 | 97 | 50 | 50 ± 2 | 100 |
| | 100 | 106 ± 6 | 99 | 100 | 99 ± 4 | 99 |
| Ni | — | 60 ± 3 | — | — | 0.04 ± 0.001 | — |
| | 50 | 111 ± 5 | 102 | 50 | 49 ± 2 | 98 |
| | 100 | 158 ± 6 | 98 | 100 | 100 ± 3 | 100 |
| As | — | — | — | — | — | — |
| | 50 | 48 ± 3 | 96 | 50 | 50 ± 3 | 100 |
| | 100 | 96 ± 5 | 96 | 100 | 98 ± 4 | 98 |
| Al | — | 1.4 ± 0.01 | — | — | — | — |
| | 50 | 51 ± 3 | 99 | 50 | 50 | 100 |
| | 100 | 100 ± 4 | 99 | 100 | 100 | 100 |
| Co | — | 6.54 ± 0.26 | — | — | 1.86 ± 0.01 | — |
| | 50 | 55 ± 2 | 97 | 50 | 51 ± 2 | 98 |
| | 100 | 107 ± 4 | 100 | 100 | 102 ± 3 | 100 |
| Cd | — | — | — | — | — | — |
| | 50 | 49 ± 2 | 98 | 50 | 50 ± 2 | 100 |
| | 100 | 101 ± 3 | 101 | 100 | 100 ± 2 | 100 |
| Hg | — | — | — | — | — | — |
| | 50 | 47 ± 3 | 94 | 50 | 49 ± 2 | 98 |
| | 100 | 98 ± 4 | 98 | 100 | 98 ± 4 | 98 |

[a] Below detection limit. [b] $\bar{X} \pm s$.

Table 7 Concentration of the metals in water samples ($n = 3$)[a]

| Concentration, $\bar{X} \pm s$ (μg $L^{-1}$) | | | | | | | | |
|---|---|---|---|---|---|---|---|---|
| | NiF:$Pr^{3+}$–MCM-41 | | | | CoF:$Pr^{3+}$–MCM-41 | | | |
| | Cr | Pb | Ni | As | Al | Co | Cd | Hg |
| Raw wastewater | — | 6.77 ± 0.18 | 68 ± 3 | — | 0.79 ± 0.01 | 5.42 ± 0.26 | 0.39 ± 0.06 | 0.62 ± 0.01 |
| Nanofiber-membrane-treated wastewater | 7.86 ± 0.41 | 10.1 ± 1.1 | 115 ± 6 | 0.13 ± 0.01 | 8.87 ± 0.15 | 32.5 ± 1.1 | 0.85 ± 0.01 | 1.56 ± 0.01 |
| Sea mucilage | 3.16 ± 0.18 | 5.81 ± 0.02 | 3.74 ± 0.17 | — | 1.24 ± 0.02 | 23.1 ± 0.9 | 1.19 ± 0.09 | — |
| Tap water | — | — | 0.02 ± 0.001 | — | — | 0.56 ± 0.01 | — | — |

[a] Below detection limit.

removal efficiency observed under low organic-content conditions may be attributed to the concentration-dependent limitations, which are consistent with behaviors reported in the literature.

### 3.12. Analytical figures of merit

After the optimization of the experimental parameters, the analytical properties of the developed magnetic d-μSPE procedure were investigated. The limit of detection (LOD), preconcentration factor (PF), precision, and linearity of the developed method for the Cr, Pb, Ni, As, Al, Co, Cd, and Hg ions were investigated.

The limit of detection (LOD) test was performed by applying the optimized magnetic d-μSPE method combined with ICP-MS to ten 25 mL blank ($n = 10$) solutions. The LOD is defined as $C_{LOD} = 3S_b/b$, where $S_b$ is the standard deviation of the blank signals, and $b$ is the slope of the calibration curve. The LOD values for Cr, Pb, Ni, As, Al, Co, Cd, and Hg were calculated to be 0.003 μg $L^{-1}$ for Cr, 0.004 μg $L^{-1}$ for Pb, 0.002 μg $L^{-1}$ for Ni, 0.01 μg $L^{-1}$ for As, 0.01 μg $L^{-1}$ for Al, 0.001 μg $L^{-1}$ for Co, 0.002 μg $L^{-1}$ for Cd, and 0.08 μg $L^{-1}$ for Hg. The pre-concentration factor and precision of the method were found to be 250-fold and ≤2.8, respectively.

The calibration curves using eight standards for Cr, Pb, Ni, As, Al, Co, Cd, and Hg showed good linearity. The determination coefficients of the calibration curves across the range of 0–50 μg $L^{-1}$ for Cr, Pb, Ni, As, Al, Co, Cd, and Hg were higher than 0.997. The internal standards, $^{45}Sc$, $^{209}Bi$, and $^{103}Rh$, were used to ensure the stability of the instrument and to check for instrumental drift and nonspectral interferences.

### 3.13. Accuracy of the method and analysis of samples

The developed magnetic d-μSPE method was verified by the analysis of certified reference materials (CWW-TMD, wastewater). Three parallel analyses were performed for each concentration level. The analysis results of the CRMs are given in Table 5. The analyte concentrations found by the developed magnetic d-μSPE method were in good agreement with the certified values. The relative error was found to be ≤5%. The developed magnetic d-μSPE method is accurate and has high applicability for wastewater.

Also, recovery experiments with wastewater and tap water samples were performed, which included different sample matrices that were spiked with two different concentrations of metal ions. The results are given in Table 6. The recoveries (%) varied from 94% to 102% and from 98% to 100% for wastewater and tap water samples, respectively. The CRMs and recovery results indicate that the magnetic d-μSPE can be successfully used as an accurate, selective and reliable method for Cr, Pb, Ni, As, Al, Co, Cd, and Hg determination in samples with a complex matrix.

The method was extended for the magnetic d-μSPE determination of Cr, Pb, Ni, As, Al, Co, Cd, and Hg in wastewater, sea mucilage, and tap water samples. The water samples for analysis were prepared as described in Section 2.6. The results are shown in Table 7.

Table 8 Comparison of the magnetic d-μSPE methods reported on nano-sized adsorbents for the recovery of Cr, Pb, Ni, As, Al, Co, Cd, and Hg

| Adsorbent/determination technique | Analytes | pH | Pre-concentration factor | Detection limit (μg $L^{-1}$) | Adsorption capacity (mg $g^{-1}$) | RSD (%) | Adsorbent amount (mg) | Sample | References |
|---|---|---|---|---|---|---|---|---|---|
| Magnetic MOF nanocomposite/FAAS | Cd(II), Pb(II), Zn(II), and Cr(III) | 5.9 | — | 0.12, 0.7, 0.16, and 0.4 | 175 Cd(II), 168 Pb(II), 210 Zn(II), and 196 Cr(III) | ≤7.2 | 30 | Vegetable | 57 |
| $NH_2$–MCM-41 grafted membrane | Cr(VI) and Cu(II) | 11 | — | — | 2.8 Cr and 3.7 Cu | — | — | Wastewater | 58 |
| Polyethyleneimine@MCM-41 | Cu, Ni, and Cd | 3.23 | — | — | Cu, Ni, Cd: 39.30, 33.61, and 21.10, respectively | — | — | Wastewater | 59 |
| Fe/Mg–MCM-41/AAS, ICP-OES | As(V) | 3 | — | — | 71.53 | — | 0.5 g $L^{-1}$ | Wastewater | 60 |
| Chitosan/Al–MCM-48 | As(V) | 9 | — | — | 178.6 | — | — | Wastewater | 61 |
| $MnFe_2O_4$–MCM-41–SH/HG-AFS | Sb(III) | 3–11 | — | — | 164.8 | — | — | Wastewater | 62 |
| Ni/CoF:$Pr^{3+}$–M@PVDF | Cr, Pb, Ni, As, Al, Co, Cd, and Hg | 2 and 4 | 250 | 0.003 Cr, 0.004 Pb, 0.002 Ni, 0.01 As, 0.01 Al, 0.001 Co, 0.002 Cd, and 0.08 Hg | 14.9 Cr, 12.3 Pb, 10.8 Ni, 8.67 As, 32.9 Al, 13.4 Co, 28.4 Cd, and 23.5 Hg | ≤2.8 | 25 and 100 | Wastewater, sea mucilage, and tap water | This work |

## 4. Conclusions

Water analysis is a crucial component of the chemical analysis of environmental samples. The development of new methods for water analysis and the improvement of existing ones are significant tasks for analytical chemists.

In this study, a fast, sensitive, simple, low-cost, and time-saving magnetic d-μSPE procedure was developed for the ICP-MS determination of Cr, Pb, Ni, As, Al, Co, Cd, and Hg elements in industrial wastewater, sea mucilage, and tap water samples using magnetic Ni/CoF:$Pr^{3+}$–M@PVDF nanofiber membranes. Additionally, the application of the synthesized nanofiber membranes to remove biological and organic pollutants in industrial wastewater samples was investigated. For this reason, the magnetic Ni/CoF:$Pr^{3+}$–M@PVDF nanofiber membranes were synthesized and used for the first time as an adsorbent for the magnetic d-μSPE determination of Cr, Pb, Ni, As, Al, Co, Cd, and Hg elements, as well as organic and biological pollutants in industrial wastewater. XRD analyses confirmed the formation of the spinel $NiFe_2O_4$ and $CoFe_2O_4$ structures, together with the preserved amorphous MCM-41 framework, while revealing the presence of Pr and Fe oxide secondary phases. Although minor secondary phases, such as $\alpha$-$Fe_2O_4$ and Pr-containing oxides, are detected in the XRD patterns, the spinel ferrite phase remains dominant and is primarily responsible for the magnetic properties of the materials. The presence of these secondary phases may lead to a slight reduction in the overall magnetization; however, due to their low abundance, they do not significantly hinder the magnetic separation performance. In practical applications, rapid and efficient magnetic separation was consistently achieved, indicating that the materials retain sufficient magnetic responsiveness. Moreover, the reproducibility of the extraction results demonstrates that the multiphase composition does not adversely affect the functional stability of the system. These structural findings confirm that the synthesized nanocomposites exhibit the requisite crystallographic features to ensure a strong magnetic response and high adsorption performance in the d-μSPE process.

A comparison of the analytical performance of the developed magnetic d-μSPE method with those reported using some nanosized adsorbents for the analysis of Cr, Pb, Ni, As, Al, Co, Cd, and Hg is shown in Table 8.[57–62] When compared with the other methods using nano-sized adsorbents, the Ni/CoF:$Pr^{3+}$–M@PVDF nanofiber membranes exhibit fast adsorption and elution kinetics, higher adsorption capacities, relatively high reusability for a magnetic adsorbent (60), low detection limits, and a good pre-concentration factor (250). This approach is time-efficient due to the magnetically assisted separation procedure. The recovery values for Cr, Pb, Ni, As, Al, Co, Cd, and Hg in CRMs indicate that the method has good accuracy, selectivity, and reliability. The magnetic d-μSPE method can be successfully applied for the separation and pre-concentration of inorganic, biological, and organic pollutants from water samples.

For the removal of biological pollutants, *E. coli* colony counts were evaluated in influent wastewater samples. The results demonstrated that both nanofiber membrane materials substantially reduced the *E. coli* load in the influent wastewater sample. Overall, these findings indicate that NiF:$Pr^{3+}$–M@PVDF and, more notably, CoF:$Pr^{3+}$–M@PVDF possess significant potential for *E. coli* removal from influent wastewater and may serve as promising candidates for advanced microbial control strategies in the early stages of wastewater treatment.

Nanofiber-mesoporous composites have been observed to contribute to COD removal, particularly in wastewater with high organic loads. The limited removal efficiency achieved in the treated water samples with low organic-matter content is consistent with diffusion-controlled mass transfer, as described in the literature. Similarly, the interaction between the praseodymium-doped metal oxide structure and the electrospun fiber structure is also considered to contribute to the performance of these composites.

## Author contributions

Şerife Saçmacı: conceptualization, methodology, writing – review and editing, validation, supervision, resources. Rabia Güzel: methodology. Mustafa Saçmacı: methodology, writing – review and editing. Ruken Esra Demirdöğen: methodology, writing – review and editing. Aycan Gündoğdu: methodology, writing – review and editing. Nuray Ateş: methodology, writing – review and editing. Oğuzhan Taştan: methodology. Mefaret Ceylan: methodology. Fatih Mehmet Emen: methodology, writing – review and editing. Kasim Ocakoglu: methodology, writing – review and editing.

## Conflicts of interest

The authors declare the following financial interests/personal relationships, which may be considered potential competing interests: Şerife Saçmacı reports that Erciyes University provided financial support.

## Data availability

The datasets generated and/or analyzed during the current study are available from the corresponding author upon reasonable request.

## Acknowledgements

This study was supported by the Scientific Research Project Unit of the Erciyes University, Türkiye (Grant No. FOA-2019-8690).

## References

1 A. M. Dijk-Looijaard and J. Genderen, Levels of exposure from drinking water, *Food Chem. Toxicol.*, 2000, **38**, 37–42.
2 R. L. Manasa and A. Mehta, Wastewater: sources of pollutants and its remediation, in *Environmental Biotechnology*, Springer International Publishing, Cham, 2020, vol. 2, pp. 197–219.

3 United Nations Statistics Division, *System of Environmental-Economic Accounting for Water*, United Nations, New York, 2012, p. 196.
4 A. Sonune and R. Ghate, Development in wastewater treatment methods, *Desalination*, 2004, **167**, 55–63.
5 United States Environmental Protection Agency (EPA) and Office of Wastewater Management, *Primer for Municipal Wastewater Treatment*, Report Number EPA 832-R-04-001, 2004.
6 *Sick water? The central role of wastewater management in sustainable development: a rapid response assessment*, ed. E. Corcoran, C. Nellemann, E. Baker, R. Bos, D. Osborn and H. Savelli, United Nations Environment Programme, UN-HABITAT and GRID-Arendal, 2010.
7 World Health Organization, *Guidelines for drinking-water quality*, 4th edn, 2011.
8 R. Baum, J. Luh and J. Bartram, Sanitation: a global estimate of sewerage connections without treatment and the resulting impact on MDG progress, *Environ. Sci. Technol.*, 2013, **47**, 1994–2000.
9 H. Shuval, Estimating the global burden of thalassogenic diseases: human infectious diseases caused by wastewater pollution of the marine environment, *J. Water Health*, 2003, **1**(2), 53–64.
10 G. Ochieng, E. Seanego and O. Nkwonta, Impacts of mining on water resources in South Africa: a review, *Sci. Res. Essays*, 2010, **5**, 3351–3357.
11 A. Bhatnagar, V. J. P. Vilar, C. M. S. Botelho and R. A. R. Boaventura, A review of the use of red mud as adsorbent for the removal of toxic pollutants from water and wastewater, *Environ. Technol.*, 2011, **32**, 231–249.
12 M. M. El-Moselhy, A. K. Sengupta and R. Smith, Carminic acid modified anion exchanger for the removal and pre-concentration of Mo(VI) from wastewater, *J. Hazard. Mater.*, 2011, **185**, 442–446.
13 C. A. R. Reyes and L. Y. V. Fiallo, Application of illite- and kaolinite-rich clays in the synthesis of zeolites for wastewater treatment, *Earth Environ. Sci.*, 2011, 363–374.
14 H. Abdolmohammad-Zadeh and Z. Talleb, Magnetic solid phase extraction of gemfibrozil from human serum and pharmaceutical wastewater samples utilizing a β-cyclodextrin grafted graphene oxide-magnetite nano-hybrid, *Talanta*, 2015, **134**, 387–393.
15 S. Ma, M. He, B. Chen, W. Deng, Q. Zheng and B. Hu, Magnetic solid phase extraction coupled with inductively coupled plasma mass spectrometry for the speciation of mercury in environmental water and human hair samples, *Talanta*, 2016, **146**, 93–99.
16 D. H. K. Reddy and Y. S. Yunang, Spinel ferrite magnetic adsorbents: alternative future materials for water purification?, *Coord. Chem. Rev.*, 2016, **315**, 90–111.
17 R. Valenzuela, Novel applications of ferrites, *Phys. Res. Int.*, 2012, 1–9.
18 G. Litsardakis, I. Manolakis, C. Serletis and K. G. Efthimiadis, Effects of Gd substitution on the structural and magnetic properties of strontium hexaferrites, *J. Magn. Magn. Mater.*, 2007, **316**, 170–173.
19 D. Mehta, S. Mazumdar and S. K. Singh, Magnetic adsorbents for the treatment of water/wastewater: a review, *J. Water Process Eng.*, 2015, **7**, 244–265.
20 G. R. Chaudhary, P. Saharan, A. Kumar, S. K. Mehta, S. Mor and A. Umar, Adsorption studies of cationic, anionic and azo-dyes via monodispersed $Fe_3O_4$ nanoparticles, *J. Nanosci. Nanotechnol.*, 2013, **13**, 3240–3245.
21 V. K. Sharma, T. J. Mcdonald, H. Kim and V. K. Garg, Magnetic graphene – carbon nanotube iron nanocomposites as adsorbents and antibacterial agents for water purification, *Adv. Colloid Interface Sci.*, 2015, **225**, 229–240.
22 L. H. J. Lajunen, *Spectrochemical Analysis by Atomic Absorption and Emission*, Finland, 1991, pp. 215–225.
23 A. Gündoğdu, A. V. Jennison, H. V. Smith, H. Stratton and M. Katouli, Extended-spectrum β-lactamase producing Escherichia coli in hospital wastewaters and sewage treatment plants in Queensland, Australia, *Can. J. Microbiol.*, 2013, **59**(11), 737–745.
24 B. Aydemir, Synthesis of Mesoporous Catalysts and Their Performance in Pyrolysis of Polyethylene, Master's thesis, METU, 2010.
25 A. Ziarati, A. Sobhani-Nasab, M. Rahimi-Nasrabadi, M. R. Ganjali and A. Badiei, Sonication method synergism with rare earth based nanocatalyst: preparation of $NiFe_{2-x}Eu_xO_4$ nanostructures and its catalytic applications for the synthesis of benzimidazoles, benzoxazoles, and benzothiazoles under ultrasonic irradiation, *J. Rare Earths*, 2017, **35**, 374–381.
26 American Public Health Association, American Water Works Association and Water Environment Federation, *Method 5220 D, Chemical Oxygen Demand. Standard Methods for the Examination Water and Wastewater*, American Public Health Association, American Water Works Association and Water Environment Federation, Washington DC, Denver and Alexandria, USA, 2017.
27 T. M. Naidu and P. L. Narayana, Synthesis and characterization of Fe-$TiO_2$ and $NiFe_2O_4$ nanoparticles and its thermal properties, *J. Nanosci. Technol.*, 2019, 769–772.
28 J. Mokrzycki, M. Fedyna, D. Duraczyńska, M. Marzec, R. Panek, W. Franus, T. Bajda and R. Karcz, Mesoporous silica MCM-41 from fly ash as a support of bimetallic Cu/Mn catalysts for toluene combustion, *Materials*, 2024, **17**(3), 653.
29 K. Kombaiah, J. J. Vijaya, L. J. Kennedy, M. Bououdina, R. J. Ramalingam and H. A. Al-Lohedan, Comparative investigation on the structural, morphological, optical, and magnetic properties of $CoFe_2O_4$ nanoparticles, *Ceram. Int.*, 2017, **43**(10), 7682–7689.
30 M. Thommes, K. Kaneko, A. V. Neimark, J. P. Olivier, F. Rodriguez-Reinoso, J. Rouquerol and K. S. W. Sing, Physisorption of gases, with special reference to the evaluation of surface area and pore size distribution (IUPAC Technical Report), *Pure Appl. Chem.*, 2015, **87**(9–10), 1051–1069.
31 S. Jana, B. Dutta, H. Honda and S. Koner, Mesoporous silica MCM-41 with rod-shaped morphology: synthesis and characterization, *Appl. Clay Sci.*, 2011, **54**(2), 138–143.

32 M. Thommes, K. Kaneko, A. V. Neimark, J. P. Olivier, F. Rodriguez-Reinoso, J. Rouquerol and K. S. W. Sing, Physisorption of gases, with special reference to the evaluation of surface area and pore size distribution (IUPAC Technical Report), *Pure Appl. Chem.*, 2015, **87**(9–10), 1051–1069.
33 M. M. El-Masry and M. M. Arman, Cobalt, nickel and zinc spinel ferrites with high transmittance and UV-blocking for advanced optical applications, *Sci. Rep.*, 2025, **15**, 16636.
34 R. D. Shannon, Revised effective ionic radii and systematic studies of interatomic distances in halides and chalcogenides, *Acta Crystallogr. Sect. A Cryst. Phys. Diffr. Theor. Gen. Crystallogr.*, 1976, **32**(5), 751–767.
35 Z. Peng, X. Fu, H. Ge, Z. Fu, C. Wang, L. Qi and H. Miao, Effect of $Pr^{3+}$ doping on magnetic and dielectric properties of Ni–Zn ferrites by "one-step synthesis", *J. Magn. Magn. Mater.*, 2011, **323**(20), 2513–2518.
36 M. M. El-Masry and M. M. Arman, Cobalt, nickel and zinc spinel ferrites with high transmittance and UV-blocking for advanced optical applications, *Sci. Rep.*, 2025, **15**, 16636.
37 S. M. Holmes, V. L. Zholobenko, A. Thursfield, R. J. Plaisted, C. S. Cundy and J. Dwyer, In situ FTIR study of the formation of MCM-41, *J. Chem. Soc., Faraday Trans.*, 1998, **94**, 2025.
38 X. S. Zhao and G. Q. Lu, Modification of MCM-41 by Surface Silylation with Trimethylchlorosilane and Adsorption Study, *J. Phys. Chem. B*, 1998, **102**(9), 1556–1561.
39 B. Gillot and B. Domenichini, Effect of the preparation method and grinding time of some mixed valency ferrite spinels on their cationic distribution and thermal stability toward oxygen, *Mater. Chem. Phys.*, 1996, **47**, 217–224.
40 S. Zhang, M. Perez-Page, K. Guan, E. Yu, J. Tringe, R. H. R. Castro, R. Faller and P. Stroeve, Response to Extreme Temperatures of Mesoporous Silica MCM-41: Porous Structure Transformation Simulation and Modification of Gas Adsorption Properties, *Langmuir*, 2016, **32**(44), 11422–11431.
41 J. O. Ighalo, F. O. Omoarukhe, V. E. Ojukwu, K. O. Iwuozor and C. A. Igwegbe, Cost of adsorbent preparation and usage in wastewater treatment: a review, *Cleaner Chemical Engineering*, 2022, **3**, 100042.
42 R. S. Yadav, J. Havlica, I. Kuritka, Z. Kozakova, J. Masilko, M. Hajduchova, V. Enev and J. Wasserbauer, Effect of $Pr^{3+}$ Substitution on Structural and Magnetic Properties of $CoFe_2O_4$ Spinel Ferrite Nanoparticles, *J. Supercond. Novel Magn.*, 2014, **28**(1), 241–248.
43 Ş. Saçmacı and M. Saçmacı, The rapid determination of lead in food samples by magnetic dispersive solid-phase extraction coupled zeta potential analyzer, *Int. J. Environ. Anal. Chem.*, 2022, **102**(16), 4451–4465.
44 A. E. Nel, L. Mädler, D. Velegol, T. Xia, E. M. V. Hoek, P. Somasundaran, F. Klaessing, V. Castranova and M. Thompson, Understanding biophysicochemical interactions at the nano–bio interface, *Nat. Mater.*, 2009, **8**(7), 543–557.
45 M. Mahmoudi, S. Sant, B. Wang, S. Laurent and T. Sen, Superparamagnetic iron oxide nanoparticles (SPIONs): development, surface modification and applications in chemotherapy, *Adv. Drug Delivery Rev.*, 2011, **63**(1–2), 24–46.
46 L. H. Reddy, J. L. Arias, J. Nicolas and P. Couvreur, Magnetic nanoparticles: design and characterization, toxicity and biocompatibility, *Chem. Rev.*, 2012, **112**(11), 5818–5878.
47 Q. Li, S. Mahendra, D. Y. Lyon, L. Brunet, M. V. Liga, D. Li and P. J. J. Alvarez, Antimicrobial nanomaterials for water disinfection and microbial control: potential applications and implications, *Water Res.*, 2008, **42**(18), 4591–4602.
48 S. M. Dizaj, F. Lotfipour, M. Barzegar-Jalali, M. H. Zarrintan and K. Adibkia, Antimicrobial activity of the metals and metal oxide nanoparticles, *Mater. Sci. Eng., C*, 2014, **44**, 278–284.
49 H. Zhang, J. A. Smith and V. Oyanedel-Craver, The effect of natural water conditions on the anti-bacterial performance and stability of silver nanoparticles capped with different polymers, *Water Res.*, 2012, **46**(3), 691–699.
50 G. R. Reddy, K. Chennakesavulu, P. Lakshmipathiraj, B. Ravindran, S. W. Chang, S. M. Lee, P. N. Tri and D. D. Nguyen, Removal of organic pollutants in water by the MCM-41 anchored with nickel(II) and copper(II) complexes, *Environ. Technol. Innovat.*, 2021, **22**, 101492.
51 M. Bahrami and Z. Derikvand, Fabrication of a new magnetic $CoFe_2O_4$/ZrMCM-41 nanocomposite: simple construction and application for fast reduction of Cr(IV) and nitroaromatic compounds, *J. Mol. Struct.*, 2022, **1254**, 132367.
52 H. Chen, M. Huang, Y. Liu, L. Meng and M. Ma, Functionalized electrospun nanofiber membranes for water treatment: a review, *Sci. Total Environ.*, 2020, **739**, 139944.
53 Y. Tang, Z. Cai, X. Sun, C. Chong, X. Yan, M. Li and J. Xu, Electrospun nanofiber-based membranes for water treatment, *Polymers*, 2022, **14**(10), 2004.
54 Y. S. Ho and G. McKay, Pseudo-second order model for sorption processes, *Process Biochem.*, 1999, **34**(5), 451–465.
55 K. Y. Foo and B. H. Hameed, Insights into the modeling of adsorption isotherm systems, *Chem. Eng. J.*, 2010, **156**(1), 2–10.
56 D. P. Sahoo, D. Rath, B. Nanda and K. M. Parida, Transition metal/metal oxide modified MCM-41 for pollutant degradation and hydrogen energy production: a review, *RSC Adv.*, 2015, **5**(102), 83707–83724.
57 A. Hassanpour, R. Hosseinzadeh-Khanmiri, M. Babazadeh, J. Abolhasani and E. Ghorbani-Kalhor, Determination of heavy metal ions in vegetable samples using a magnetic metal–organic framework nanocomposite sorbent, *Food Addit. Contam.*, 2015, **32**(5), 725–736.
58 Y. Bao, X. Yan, W. Du, X. Xie, Z. Pan, J. Zhou and L. Li, Application of amine-functionalized MCM-41 modified ultrafiltration membrane to remove chromium(VI) and copper(II), *Chem. Eng. J.*, 2015, **281**, 460–467.
59 S. Li, L. Wang, P. Lu, Y. Li, Y. Li, Y. Wang and D. Qiu, Nanoconfined polyethyleneimine in mesoporous MCM-41 silica for heavy metal ions removal, *Sep. Purif. Technol.*, 2025, **353**, 128421.

60 Y. Song, P. Huang, H. Li, R. Li, W. Zhan, Y. Du, M. Ma, J. Lan, T. C. Zhang and D. Du, Uptake of arsenic(V) using iron and magnesium functionalized highly ordered mesoporous MCM-41 (Fe/Mg-MCM-41) as an effective adsorbent, *Sci. Total Environ.*, 2022, **833**, 154858.

61 M. R. Abukhadra, F. M. Dardir, E. A. Ahmed, M. F. Soliman, S. I. Othman, A. A. Allam, W. A. Zoubi and M. S. Shaban, Insight into the Influence of the Integrated Chitosan on the Adsorption Properties of Chitosan/Al-MCM-41 Composite for As(V) Metal Ions: Characterization and Advanced Equilibrium Studies, *Nanomater. Nanotechnol.*, 2023, **1**, 9879371.

62 W. Li and F. Fu, Incorporating $MnFe_2O_4$ onto the thiol-functionalized MCM-41 for effective capturing of Sb(III) in aqueous media, *Microporous Mesoporous Mater.*, 2020, **298**, 110060.